Vortex dynamics and fin-fin interactions resulting in performance enhancement in fish-like propulsion

Jiacheng Guo (郭佳诚), Pan Han (韩攀), Wei Zhang (张伟), Junshi Wang (王君实), George V. Lauder, Valentina Di Santo, and Haibo Dong (董海波)

Phys. Rev. Fluids **8**, 073101 — Published 21 July 2023

DOI: 10.1103/PhysRevFluids.8.073101

Vortex dynamics and fin-fin interactions resulting in performance enhancement in fish-like propulsion

Jiacheng Guo[1], Pan Han[1], Wei Zhang[1], Junshi Wang[1, 2], George V. Lauder[3], Valentina Di Santo[4], Haibo Dong[1, *]

[1] *Department of Mechanical and Aerospace Engineering, University of Virginia, Charlottesville, VA 22903, USA*

[2] *Present address: Department of Mechanical and Aerospace Engineering, Princeton University, Princeton, NJ 08544*

[3] *Museum of Comparative Zoology, Harvard University, Cambridge, MA 02138, USA*

[4] *Division of Functional Morphology, Department of Zoology, Stockholm University, SE-11418, Stockholm, Sweden*

The leading-edge vortex (LEV) formation on the caudal fin (CF) has been identified to play a key role in efficient lift-based thrust production of fish-like propulsion. The enhancement of CF LEV through its interaction with vortices formed upstream due to a median fin with a distinct shape is the focus of this study. High-speed, high-fidelity videos and particle imaging velocimetry (PIV) were obtained from rainbow trout during steady forward swimming, to visualize the undulatory kinematics and 2-dimensional (2-D) flow behavior. Body kinematics are quantified using a traveling-wave formulation that is used to prescribe the motion of a high-fidelity 3-dimensional (3-D) surface model of fish body for a computational fluid dynamics (CFD) study. The pressure field of the CFD result is compared and validated with the PIV result from the experiment. Using CFD, the vortex forming and shedding behaviors of the anal fin (AF), and their capturing and interaction with the trunk (TK) and the CF are visualized and examined. Coherent anal-fin-bound leading-edge vortices (AF-LEV) are found to form periodically, leading to AF's thrust production. The vortices subsequently shed from the AF are found to help stabilize and reinforce the leading-edge vortex (LEV) formation on the CF by aiding LEV initiation at stroke reversal and enhancing LEV during a tail stroke, which leads to enhancement of lift-based thrust production. The CF is found to shed vortex tubes (VT) that create backward-facing jets, and the ventral-side VT and the associated backward jets are both strengthened by vortices shed by AF. An additional benefit of the AF is found to be reduction of body drag by reducing the lateral crossflow that leads to loss of beneficial pressure gradient across the body. Through varying AF-CF spacing and AF height, we find that CF thrust enhancement and trunk drag reduction due to AF are both affected by the position and size of the AF. The position and area of the anal fin that led to the most hydrodynamic benefit are found to be the original, anatomically accurate position and size. This work demonstrates the important effect of vortex interaction among propulsive surfaces in fish-like propulsion.

[*] Authors to whom correspondence should be addressed. E-mail: (H.D.) hd6q@virginia.edu

I. INTRODUCTION

The formation of leading-edge vortices (LEV) has been observed to play a crucial role in the propulsive performance of wings and fins undergoing flapping (pitching) or oscillatory (combined heaving and pitching) motion [1–6]. A computational study conducted by Borazjani and Daghooghi revealed that the oscillatory motion of the fish caudal fin creates prominent LEVs consistently over a variety of fish fin shapes [7]. In Lighthill's study of oscillating hydrofoil, it is found that fish swimming with high hydromechanical efficiency balances the two mechanisms of force production: 1) forward component of pressure difference between the two sides of the fin, and 2) leading-edge suction due to the low-pressure region created by the swirling of water around the leading edge [2]. This suction force created by leading-edge vorticity, clearly visualized computationally in Eldredge and Jones's review study of LEV formation on moving plates [4], is a well-known mechanism by which birds and insects augment their lift production [5,8–11]. Anderson et al. studying the performance of oscillating hydrofoil found that high propulsive efficiency is related to the formation of moderately strong LEVs on alternating sides of the foil [1].

The suction force created by LEV is dependent on its circulation strength [4]. To explore methods of enhancing the LEV circulation and stability, Harbig et al. conducted a computational study on a flapping plate and found that the attachment and circulation of LEV can be enhanced by an increase in advance ratio, based on a definition similar to the Strouhal number [9]. However, whether or not the LEV enhancement came at a cost of increased power consumption is not discussed, even though in oscillating foils and fish swimming, Strouhal number changes have been found to affect propulsive efficiency [1,3]. For ways to enhance both LEV and propulsive efficiency simultaneously, there is a growing interest in vortex capturing in fish-inspired locomotion [6,12–20]. Liao et al. found that by introducing vortices upstream of a live trout, the trout would adopt a gait synchronized to the upstream vortex shedding and trace the path of the vortices, a locomotion pattern that is associated with energy recovery [12,13]. Experimental and computational studies of hydrofoils in tandem formation undergoing either pure pitching or oscillation motions found that the downstream foil's performance is affected by the vortex pattern it encounters [15,16,18,20–27]. In Newbolt et al.'s study in which tandem hydrofoils were assigned uncoordinated flapping motions, the follower in the leader's wake could fall into various stable positions controlled by changes in amplitude, phase, and frequency [24]. Akhtar et al. conducted a computational bio-inspired tandem foil study, wherein the motion of the two foils is prescribed based on the motion of dorsal and caudal fins in a bluegill sunfish, finding a unique mechanism of thrust enhancement whereby the upstream fin alters the flow so that the downstream fin exhibits a larger angle of incidence, and thus the formation and shedding of LEV on the downstream fin is enhanced [16]. In Zhang et al.'s study of fin-fin interaction using tuna-inspired fin models and kinematics, it was found that the LEV-based thrust production of the caudal fin was enhanced through encountering the same-signed vortex shed from the upstream fin [25]. In a computational study of periodically pitching tandem foils, Han et al. observed LEV enhancement in the downstream foil, and achieved a multi-fold efficiency boost by adjusting the relative flapping phases of the foil [19]. Han et al. also identified four main wake types containing combinations of

"2-S" and "2-P" vortices and their associated mean-flow jet shapes, finding the "2-P" vortices, formed due to the optimal combining of LEV and trailing-edge vortex (TEV) of the hindmost foil, to be the most closely associated with high propulsive efficiency [19]. The optimal vortex capturing of a downstream foil and the propulsive performance of the whole system can depend on both the relative oscillating phase difference and the spacing between the two foils [15,18,24,25]. In Zhang et al.'s study, constructive fin-fin interaction was achieved across a wide range of spacing and phase variations, with the interaction tending to be stronger in close formations, and when the upstream fin was leading in phase [25]. In a study focusing on the hydrodynamic energy recovery of oscillating foils, Kinsey and Dumas found that the optimal positioning of the foils for energy recovery can be characterized by a "global phase" parameter that accounts for both the oscillating phase difference and the spacing between the two foils [18]. Ribeiro et al. [15] combined experimental and computational approaches and modified the "global phase" by also accounting for the inter-foil flow velocity to achieve a better prediction of the efficiency of the downstream foil and the associated energy efficiency. Overall, it is found that both foils produce thrust, and the downstream foil's propulsive efficiency is optimized when the capturing of incoming vortices enhances the LEV circulation of the downstream foil.

Observation from real fish swimming supports the hypothesis of fish propulsion benefiting from fin-fin interaction [28–31], as tandem-foil studies predict. However, it is unclear from these observations if findings from tandem-foil studies are directly applicable to real fish swimming. Pure tandem-foil configurations often neglect the existence of a trunk, which can restrict foil kinematics and alter the flow in ways unaccounted for. Matthew and Lauder navigated the existence of a trunk by constructing pitching-heaving plates specifically shaped to mimic the entire sideview silhouette of a fish containing median and caudal fins with different spacings [32]. A larger change in performance is observed in plates with varying flexibility than in plates with varying fin-fin spacing. Computationally, Liu et al. and Han et al. studied the fin-fin and fin-body interactions of the median fin, trunk and caudal fin using realistic 3-D models and undulating kinematics of jackfish and sunfish, respectively [6,33]. By constructing three different models (full-body model, model with trunk and caudal fin and without median fins, and caudal-fin-only model) the effect of fin-fin interaction on the propulsive performance of the caudal fin was isolated, and Liu et al. found that the caudal fin thrust and LEV are enhanced by the presence of the median fins, which extend and redirect trunk-bound vortices to be better accessed by the caudal fin for its own LEV formation [6]. By varying the relative phase difference between the median and caudal fins, Han et al. found that the phase-lead exhibited by the median fins can better enhance the caudal fin's LEV [33]. However, in both cases, differing from the thrust producing leading foils in tandem-foil studies, the median fins serve only to extend the vortices that originate on the trunk, and no median-fin propulsive performance or vortex generation independent of the trunk was discussed.

This study aims to further elucidate the flow physics behind the enhancement of LEV due to fin-fin interactions, and its benefits to performance in both thrust production and energetics, using a realistic trout-like model, which

exhibits an anal fin that extends far and has a shape distinct from the outline of the trunk, allowing it to interact with the flow more directly than jackfish and sunfish. In experimental studies of trout swimming, the anal fin is found to produce reverse von-Karman wake patterns [29,30], the interactions of which with the caudal fin and associated performance enhancement can be interesting areas of discussion. The analysis showcased in this study combines experimental and computational approaches, using experimental data on the live fish as the basis for extensive computational modelling, focusing on the interactions between the anal fin and the caudal fin. We obtained PIV data from fish swimming in a flow tank, and then flow simulation studies are conducted on a realistic 3-D trunk and fin model whose motion is based on the video recording of the fish's swimming during the PIV data collection. The simulation results are validated with the PIV data to ensure compatibility to experiments, and then used to resolve detailed flow physics and vortex dynamics. The body kinematics are governed by a traveling-wave model [33]. This traveling-wave reconstruction approach produces symmetric kinematics, somewhat simplified from the actual fish motion, that can be reduced to parametric components and easily replicated. The traveling-wave kinematics is validated against the recorded fish kinematics to ensure good agreement between the model kinematics and the true kinematics.

The spacing between the anal fin and caudal fin is varied to study its effectiveness at different positions along the body. Fish species in general and trout species particularly differ in the location of the anal fin relative to the tail, and a computational approach allows for the fine control of such a parameter. In addition, the aspect ratio of the anal fin is varied to mimic the opening and closing of the anal fin observed during fish locomotion. The outcome of this work is a characterization of flow physics involved in the interaction between trout's distinctive median and caudal fin, both exhibiting unique shapes that produce vortex structures and interactions previously undiscussed, leading to a more complete understanding of LEV-based thrust and propulsive efficiency enhancement through vortex interactions. This combination of experimental data from live fish and computational simulations is also conducive to designing efficient biomimetic fish-like robots and AUVs [34,35].

The organization of subsequent sections is follows. Section II-A will describe the setup of experiments for PIV data collection and video recording. Section II-B describes the computational model and body kinematics. Section II-C describes the simulation setup and flow solver. The results of the PIV-computation validation are shown in section II-C. Section III-A compares the hydrodynamic performance and vortex structures of the full-body model (M1) and the model without the anal fin (M2). Sections III-B and III-C, respectively, compare the performance and vortex structures among models with varying spacing between the anal fin and caudal fin, and among models with varying anal fin aspect ratios.

II. METHODOLOGY

A. Set-up for experimental data collection

Experiments on live rainbow trout (*Oncorhynchus mykiss*) swimming steadily included video recording and particle image velocimetry (PIV) data acquisition. The fish swam in a recirculating flow tank using setups described

in studies conducted by Drucker and Lauder, Standen and Lauder, Matthews and Lauder, and Di Santo et al. [29,30,32,36]. Briefly, live fish 11-15 cm in body length swam against an imposed flow that ranged from 0.5 to 2.0 body lengths per second (L_B/s) in a flow tank with cross-sectional area of $30\ \mathrm{cm}^2$ and a working section length of 100 cm. Three synchronized high-speed cameras (Photron mini-AX200, 1024 by 1024-pixel resolution) were used to capture swimming kinematics of both the body and anal fin from the lateral, ventral and posterior views at 250 frames per second. Posterior-view video visualization of the deformation and relative phase difference between fins were aided by a mirror using a setup described in Ref. [28,37,38]. Small near-neutrally buoyant $50\ \mu\mathrm{m}$ particles were added to the recirculating flow tank and illuminated with two 5W argon ion lasers (Optoengine Inc.). Use of two lasers one illuminating the body from the left side and the other from the right side, minimized regions with poor illumination. The particle flow over the fish was visualized with a ventral view camera at 1280×1024 pixel resolution filming at a rate of 1000 frames per second. The resulting high-speed videos of particle flow patterns were analyzed using Davis v8.3 software (LaVision Inc.) using the same parameters as in recent studies of aquatic locomotion [32,39–41]: 50% interrogation window overlap and sequential image cross-correlation.

High-fidelity reconstruction of the undulatory kinematics of the fish swimming is done based on the video recording of a representative undulating cycle. A selection of frames of video recording during such an undulating cycle are shown in the ventral view in Fig. 1 (a1, b1). On Autodesk Maya, an anatomically realistic virtual skeleton and 3-D surface model are constructed based on the individual fish in the video recording. A Catmull-Clark subdivision method used in the meshing of the 3-D surface and membranes ensures the smoothness of the surfaces of the fish model. Figure 1 (a2, b2) shows a basic, rectangular surface mesh that subdivides the TK surface. This rectangular mesh is then further subdivided, refined, and triangulated to achieve the computationally robust 3-D mesh shown in Fig. 1 (a3, b3). The accuracy and compatibility of the current triangular surface mesh and computational solver are described in more detail in Ref. [42]. A skeleton-based method with calibration in a virtual scene, a technique proven accurate in reconstruction of the kinematics of jackfish undulation [6] and hummingbird flapping [43], is used for the undulatory kinematics reconstruction. The accuracy of this reconstruction method has been studied and described in detail by Koehler et al. [44]. The virtual skeleton, set up based on fish anatomy with individual vertebral segments along the body axis, allows for fine tuning of minute deformations of the 3-D model, including the bending of TK and the axial twisting of CF shown in Fig. 1 (a1-3). Rigging the virtual skeleton to the surface mesh resulted in the deformed model shown in Fig. 1 (a3) and (b3), in good agreement with the fish in the original recording.

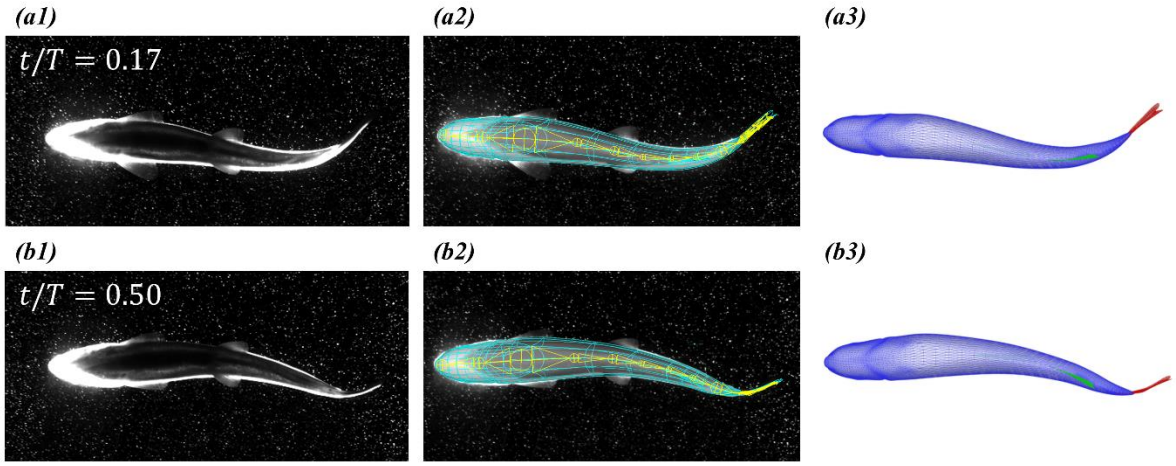

FIG. 1. (a1, b1) Original frames from the video recording taken during PIV data collection. (a2, b2) surface mesh (coarsened, and un-triangulated for visualization) is highlighted in cyan, while the virtual skeleton is highlighted in yellow. (a3, b3) fully refined and triangulated surface mesh of the fish trunk (blue) and 2-D membrane bodies representing the caudal fin (CF, red), anal fin, and dorsal fin (AF, DF, green)

B. Fish-like trunk-fin model kinematics

For the computational study, the 3-D model of the fish, shown in lateral view in Fig. 2 (a), includes the trunk (TK), caudal fin (CF), dorsal fin (DF), and anal fin (AF). TK is modelled as an enclosed surface body, while the fins are modelled as membranes, like the modelling techniques employed by Liu et al. [6]. The body undulation kinematics reconstructed from video recording is modelled using a traveling-wave formulation to quantify key characteristics in the undulating motion. The kinematics generated from the traveling-wave model is then validated against the reconstructed kinematics to ensure accuracy. Parametric studies are set up to study the effect of varying positions and sizes of the anal fin on its effectiveness and interaction with other body parts. The traveling-wave undulation model allows for the modelling of the AF motion even when its position and shape are modified. The details of the modelled undulating kinematics, its validation, and the setup of the parametric study are discussed in more detail below in this section.

Table I summarizes the key geometric parameters of the fish model, in which L_B represents the total body length of the fish, and S_{DF}, S_{AF} and S_{CF} represent surface areas of DF, AF and CF. AF-CF spacing is defined as the longitudinal distance (measured along the trunk centerline) between the leading-edge roots of AF and CF, and represented by d, as shown in Fig. 2 (b1). The AF-CF spacing of the baseline model is represented by d_0. Similarly, b_{AF} represents the AF span, while b_{AF_0} represents the AF span in the baseline model. The AF span is taken as the largest distance between the base (the line of intersection between AF and TK) and the outer edge of AF. A_{CF} represents the tip-to-tip flapping amplitude of the caudal fin, defined in Fig. 2 (c).

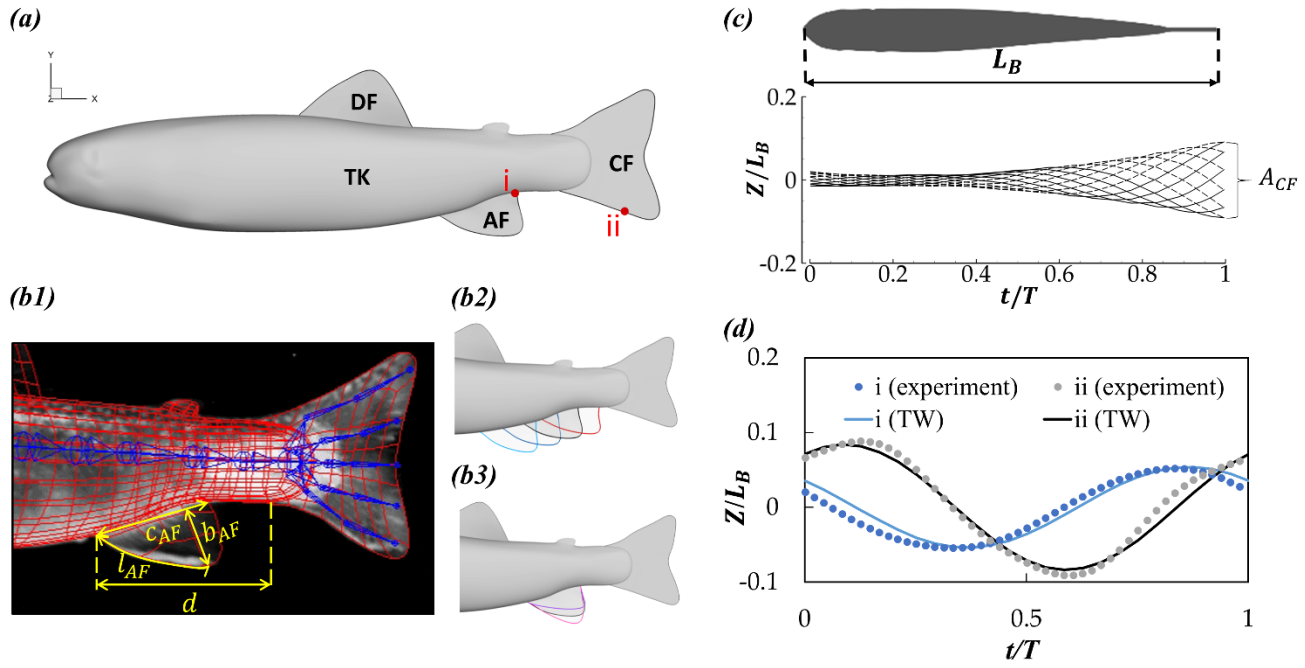

FIG. 2 (a) Lateral of the computational model with abbreviations of body parts labelled. (b) parametric study setup with (b1) defining key geometric parameters on a coarse mesh model overlaid on a picture of the real fish, (b2) demonstrating cases of varying the AF-CF spacing d to 1.5 (cyan), 1.25 (blue), and 0.75 (red) times the original position d_0. (b3) parametric study cases of varying the AF aspect ratio through variations of b_{AF} to 0.75 (purple) and 1.25 (red) times the original. (c) the midline kinematics generated by the traveling-wave model. (d) validation of the traveling wave model by tracking two points (labelled in (a)) in an entire undulation cycle, solid lines representing the traveling wave kinematics (TW), and dots representing measurements based on the video recording (experimental).

Table I. Relevant geometric parameters of the fish

L_B	$\frac{S_{DF}}{L_B^2}$	$\frac{S_{AF}}{L_B^2}$	$\frac{S_{CF}}{L_B^2}$	$\frac{d_0}{L_B}$	$\frac{b_{AF_0}}{L_B}$	$\frac{A_{CF}}{L_B}$
11 cm	0.011	0.0065	0.022	0.194	0.0634	0.19

The traveling-wave equation that governs the undulation motion of the trunk and the caudal fin is equation (1), with the term $a(x)$, defined by equation (2), a parabolic equation that defines the excursion envelope of the undulation.

$$z(x,t) = a(x) \cdot \sin\left(\frac{2\pi}{\lambda}x - 2\pi f t\right) \tag{1}$$

$$a(x) = Ax^2 + Bx + C \tag{2}$$

Here, $z(x,t)$ is the lateral excursion of a station along the fish body, as a function of x, the distance measured from the snout in the longitudinal direction when the fish is in a straightened shape, and t, time since the beginning of the current undulatory cycle. Equation (1) then describes the lateral position of a station (given by x) along the fish's midline, at a given time. Both $z(x,t)$ and x take units of L_B. Parabolic equation, $a(x)$ has coefficients $A = 0.127$, $B = -0.050$, and $C = 0.0177$. The parameter λ is the undulatory wavelength of the fish's body. Different fishes exhibit generally similar kinematic patterns regardless of body shape and undulatory modes, with wavelengths ranging from 0.50 to 1.50 L_B [36]. For the model fish in the current study, a λ of 0.8 L_B is found to produce kinematic patterns that are the most representative of the original kinematics, which is typical of a carangiform swimmer like trout [45]. The undulating frequency, f, is normalized to be 1. With the parameters given here, Fig. 2 (c) shows the midline kinematics generated by the traveling-wave formulation. The outer edges trace the parabolic curve given by equation (2). The projected length of the fish model is kept constant. This formulation does permit the length of the fish model to change slightly while undulating, but the variation is kept at a minimum. The instantaneous midline length, L, is calculated at 48 discrete timesteps during a cycle, producing a cycle average value $\bar{L}$ of 1.029, maximum value, $L_{\max}$, of 1.037, and minimum value, $L_{\min}$, of 1.021. The range of variation, $(L_{\max} - L_{\min})/\bar{L}$, is less than 1.6%. With the same method, previous works have achieved realistic fish motions and hydrodynamics [46,47].

The median fins, AF, and DF, are assigned the same frequency, f, as that of TK and CF. In the current study, to maintain lateral symmetry of the undulating kinematics, and focus on the effect of hydrodynamic interaction between AF and CF, the median-fin membranes are allowed to move passively due to the motion and curvature of the specific sections of the trunk on which the median fins are attached. To validate the traveling wave kinematic model, two points are selected (points i, and ii in Fig. 2 (a)), on the trunk and the caudal fin, at stations $x = 0.75\ L_B$ and $0.94\ L_B$, to be tracked from the video recording generated kinematics for a complete cycle. The tracked results are plotted in Fig. 2 (d) and compared with the traveling-wave equation curve. The comparison shows good agreement between the kinematics directly derived from experiments and the estimation using the equation.

The CF tip flapping amplitude A_{CF} in the traveling-wave model is $0.19\ L_B$. The non-dimensionalized parameters, Strouhal number (St) and Reynolds number (Re) are calculated, using U_∞ as the incoming flow velocity relative to the fish, and ν as the kinematic viscosity.

$$St = \frac{f A_{CF}}{U_\infty},\ Re = \frac{U_\infty L_B}{\nu} \tag{3}$$

The fish in the experiment modelled here exhibited St and Re of about 0.47 and 16000, and the fish model used for the computational study exhibits St and Re of 0.47 and 4000. For validation of CFD solver against PIV data, a higher Re of 8000 is used in the simulation. The Re used in the computational study is smaller than that encountered by the real fish in order to strike a balance between computational load and wake resolution. In Han's study as well

as Liu's study [6,33] it is found that the primary wake structure is well developed with the Re regime used in this study.

Two parametric studies are set up, visualized by Fig. 2 (b2, b3). By varying the location of the AF, shown in Fig. 2 (b2), the effect of AF-CF proximity and spacing on fin-fin interaction is studied, and by adjusting the AF height b_{AF}, shown in Fig. 2 (b3), while keeping the leading-edge arc length (l_{AF}) constant, the effect of the opening and closing of the anal fin rays is mimicked. In varying the location of the anal fin, care is taken to keep constant the base chord (c_{AF}), b_{AF}, and l_{AF}. The surface area of the anal fin (S_{AF}) variation is kept less than 4% to allow for reliable scaling of measured forces. The AF-CF spacing and AF height in the original unvaried model, d_0 and b_{AF_0} are used as baseline for comparison.

C. Numerical solver

A computational domain of size $10L_B \times 6L_B \times 6L_B$ is set up in a Euclidean space with an x-y-z coordinate system. The 3-D fish model in this domain is oriented such that it faces the negative x direction, and its dorsal fin points in the positive y direction. A Cartesian mesh is used to discretize the domain spatially. A schematic of the discretized region is shown in Fig. 3(a), in which every 2nd grid point is displayed to ensure visibility. A dense region with uniform grid spacing $\Delta x = \Delta y = \Delta z = 0.0128L_B$ is set up around the body of the fish, as indicated in the dense blue region in Fig. 3(a). The flow region ahead of the snout of the 3-D fish model is set to be $6.5L_B$ to allow the upstream flow to fully develop, leaving a region of $2.5L_B$ to capture the wake structure behind the tail, with a low stretching ratio of 0.65 such that the grid spacing at the outlet ($\Delta x = 0.08L_B$) is small enough to resolve the vortices of comparable size in that region. Additionally, near-field of the body, two nested adaptive mesh refinement (AMR) blocks are used to further refine the dense mesh to resolve the pressure and viscous forces acting on the fish body. The positions and sizes of the AMR blocks near the body are signified by purple and red outlines in the base-mesh schematic in Fig. 3 (a). A schematic of the mesh in the AMR region is also shown in Fig. 3 (a). The inner-most AMR block (red) fully bounds the fish body, and the intermediate AMR block (purple) fully contains the inner-most block, and extends another $1L_B$ in the x-direction, to resolve the finer details of the immediate wake. The smallest grid spacing inside the AMR region is equal to $0.0032\ L_B$, and the total grid count in the entire computational domain including the AMR blocks is 12 million.

To preclude the effect the grid density can have on the calculation of forces acting on the surface of the fish model, a grid-independent study is conducted on the nominal mesh described above, a coarse mesh with minimum grid spacing $\Delta x = 0.0064\ L_B$ and a dense mesh with minimum grid spacing $\Delta x = 0.0024\ L_B$. The thrust coefficient (C_T) of CF over an entire undulating cycle is calculated from simulations conducted on the three mesh setups, using equation (4),

$$C_T = \frac{-F_x}{0.5\rho U_\infty^2 S_{CF}} \tag{4}$$

where F_x is the x-directional force, with the thrust force pointing in the negative x-direction, ρ is the fluid density. The result is plotted in Fig. 3 (b). In finding that a 25% refinement of grid spacing from the nominal to the dense mesh resulted in a 1.8% C_T peak value change, we conclude that the nominal mesh is good enough for the computation, and therefore the subsequent analyses are conducted with this nominal mesh.

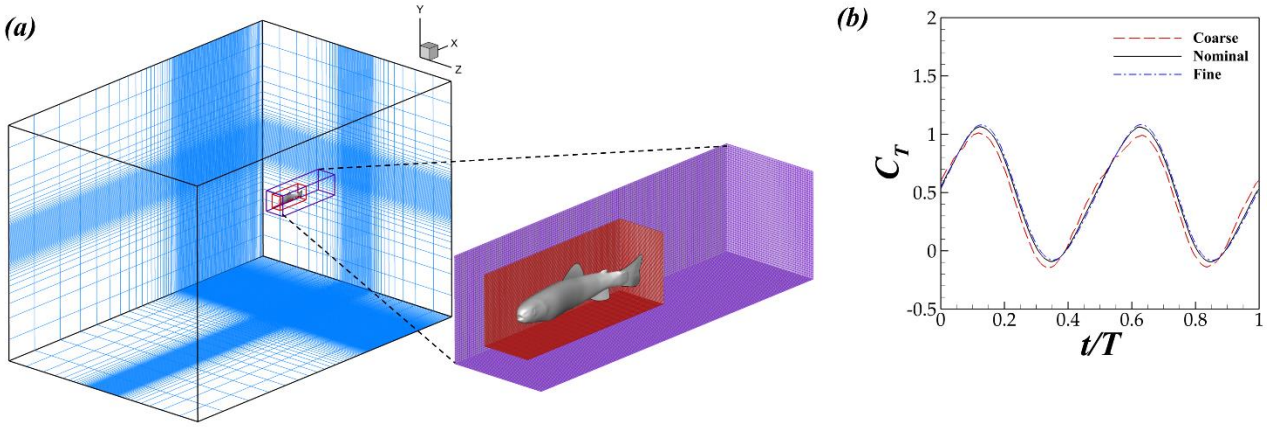

FIG. 3. Computation grid setup: (a) Nominal Cartesian grid with base mesh and nested adaptive mesh refinement (AMR) blocks, with a total grid count of 12 million. Every 2nd grid point is shown for visibility. (b) grid-dependence study with instantaneous C_T for reconstructed kinematics for a fine grid (20 million grid points), a coarse grid (7 million grid points), and the nominal grid (12 million grid points) used for subsequent analysis.

In this study, we use a direct numerical solver (DNS) to calculate Navier-Stokes Equations and resolve the fluid behavior of the swimming fish model. The same solver has successfully resolved biological flows in various cases of animal locomotion, around membranous and enclosed surfaces [5,6,10,23,48,49], and has been validated against PIV experiments in specific applications [35,50]. To verify that DNS used in this study is effective in resolving the fluid behavior in the swimming of the fish, simulation results are compared with the PIV data that are used to estimate fish body surface pressure. The velocity vector fields generated from the PIV video recordings of fish swimming (Fig. 4 (b1)) were processed according to the approach detailed in Ref. [39–41,51,52] to generate a distribution of body surface pressures shown in Fig. 4 (a1). In the simulation domain, a slice-cut is made at a location relative to the fish model similar to the horizontal laser sheet relative to the fish body in the PIV data collection, to produce the pressure and velocity vector fields shown in Fig. 4 (a2, b2). In both cases, C_P, the coefficient of pressure is calculated using $C_P = \mathrm{P}/(0.5\rho U_\infty^2)$, where P is pressure.

There is an overall good agreement between PIV and CFD results in capturing the locations and relative strengths of dominant pressure (red) and suction (blue) regions around the fish body, as seen in Fig. 4 (a1, a2). A high-pressure region directly ahead of the snout persists throughout an entire cycle of undulation and is well captured consistently by both PIV and CFD results. This is the expected result of the exposed fish snout encountering the incoming flow, causing overall drag. At the fish peduncle-tail region, a pair of high- and low-pressure regions exists, as a result of the undulation of the fish's tail, whereby the tail applies a force on the fluid

particles in its path and creates a relative vacuum in its immediate wake. Though the high- and low-pressure regions oscillate between the left and right sides of the fish peduncle-tail section due to the cyclic motion of the tail, the high-pressure (push) region remains relatively downstream and the low-pressure (suction) region remains relatively upstream of the tail, creating a persisting net forward propulsive force as the tail undergoes each stroke. Corresponding to the high-pressure region at the fish's snout in Fig. 4 (a1, a2), an overall slowdown of the flow is observed in Fig. 4 (b1, b2) in the same region. Along the fish body and CF, flow slowdown in the boundary layer is observed in both PIV and CFD results. Around the CF tip, flow from one side of the fin circulates to the other side, forming a CF-tip vortex, which is well captured by both PIV and CFD.

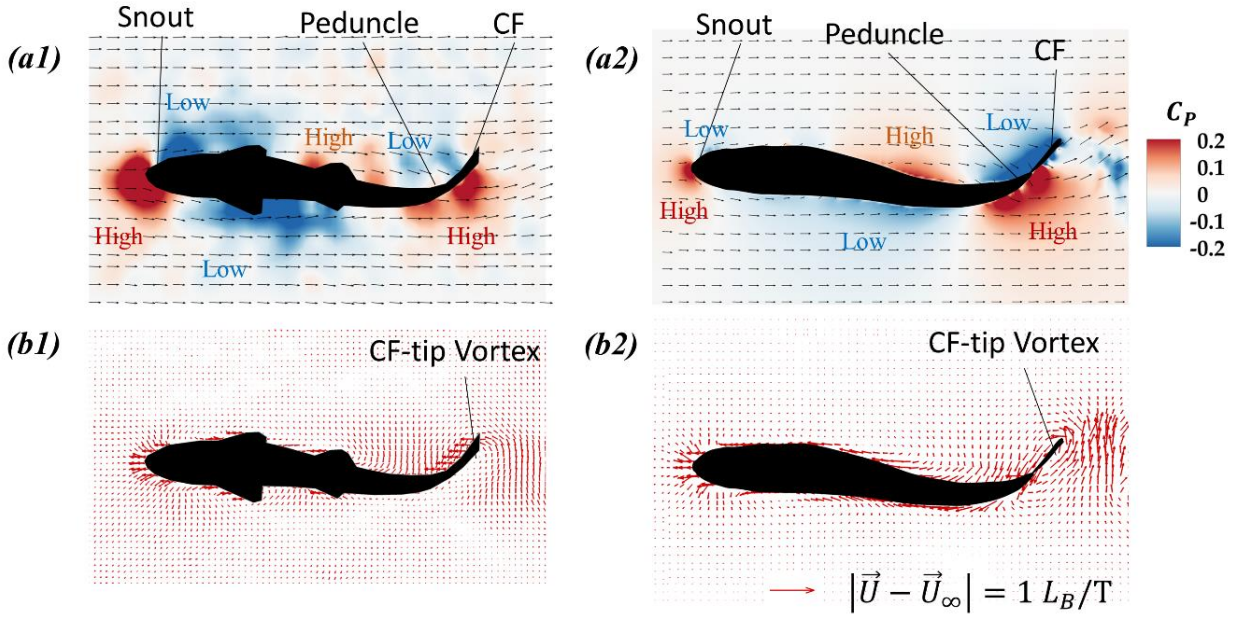

FIG. 4. (a) Pressure contour and (b) net velocity vector fields on a coronal slice cut at $t/T = 0.17$ showing (a1, b1) experimental (PIV) results, and (a2, b2) CFD results.

Besides the high-pressure region near the snout and the paired low- and high-pressure regions near the peduncle-tail section, several other regions with prominent pressure values are scattered along the trunk. The relative size and location of these regions compare well between PIV and CFD results. It should be noted that exact replication of the flow condition in the collection of PIV data was not feasible in the DNS simulation, whose Re is half the experimental value. Also, the body of the fish in the experiment includes the pectoral and pelvic fins that are excluded from the 3-D model used in the computational study to focus on resolving the flow features relevant to AF-CF interaction. Therefore, perfect quantitative agreement between experiment and simulation is not expected. Nevertheless, our DNS solver produced a flow topology that matches well with the experiment, with values in the same order of magnitude, and therefore the subsequent analyses are conducted with greater confidence using the DNS solver described in this section.

III. RESULTS AND DISCUSSION

A. Baseline performance and hydrodynamics

The time history of the coefficient of thrust (C_T) and coefficient of power consumption (C_{PW}) are shown in Fig. 5 for the trunk (TK), anal fin (AF), and caudal fin (CF) of M1 (TK+DF+AF+CF) and M2 (TK+DF+CF) for one entire undulating cycle. C_T is calculated using equation (4), and C_{PW} is calculated using equation (5), where Pw is the hydrodynamic power consumption, calculated using $Pw = \oint -(\bar{\bar{\boldsymbol{\sigma}}} \cdot \boldsymbol{n}) \cdot \boldsymbol{u}\, dS$, with $\bar{\bar{\boldsymbol{\sigma}}}$ being the local stress tensor on a body surface element with an area of dS, $\boldsymbol{n}$ is the normal vector of the surface element, and $\boldsymbol{u}$ is the velocity vector of the surface element relative to the incoming flow.

$$C_{PW} = \frac{Pw}{0.5\rho U_\infty^3 S_{CF}} \tag{5}$$

The grey region ($t/T \in [0.00, 0.50]$) signifies the rightward half stroke, during which the CF tip travels from left to right, and the white region signifies the leftward half stroke, during which the CF tip travels from right to left ending up at the position where it originated from in the undulation cycle. The general trends are qualitatively similar between the two models. Affirming numerous previous studies, CF is found to be the main propulsor, and the trunk is drag-producing. The AF at its current location is found to produce a small amount of thrust, 5.3% of total thrust in M1. AF thrust production can both contribute to propulsion in forward swimming, and aid in maneuverability, as suggested by Standen and Lauder, and Drucker and Lauder [29,30]. The cycle averaged values coefficient of thrust and power, $\bar{C}_T$ and $\bar{C}_{PW}$, are calculated. In one cycle, in the presence of AF, M1's CF produces more thrust (8.6%) than that of M2, and M1's TK produces less drag (18.6%) than that of M2. In terms of power consumption, M1's TK and CF experience marginally more hydrodynamic power consumption than M2's TK and CF, by less than 0.1% and 1.3% respectively. The AF consumes 4.6% of total power in M1. Summing the effects of TK, CF and AF for M1 and TK and CF for M2, the overall power consumption of M1 only exceeds M2 by 6%.

The most CF thrust enhancement due to AF is found to occur in the region $t/T \in (0.38, 0.65)$, during stroke reversal, while drag reduction occurs in the region of $t/T \in (0.13, 0.50)$, in during a stroke. A comparison of fluid flow and pressure fields focusing on these time periods, discussed in Fig. 9, Fig. 10, Fig. 11, can provide insight into the physics behind the AF's role in CF thrust enhancement and trunk drag reduction.

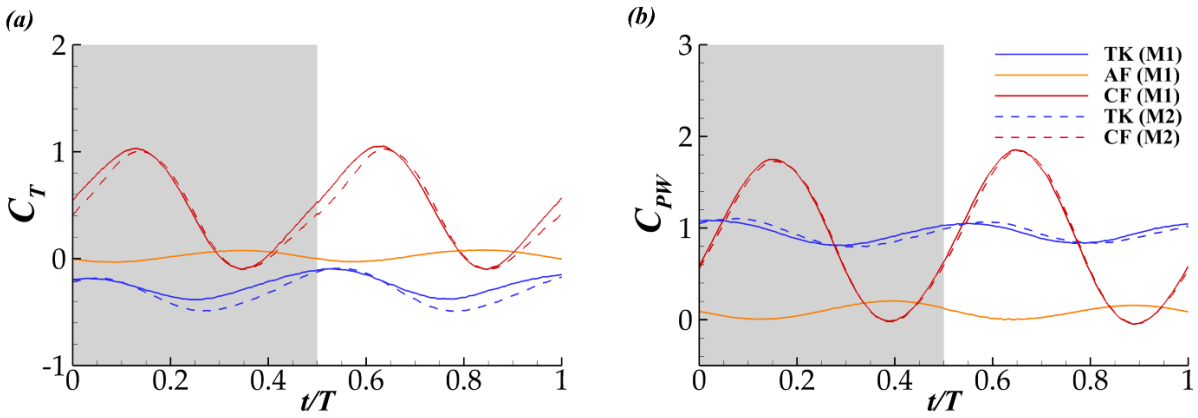

FIG. 5: Time history of (a) coefficient of thrust, and (b) coefficient of power, for M1 and M2, during one typical undulating cycle.

Towards unraveling the physics that lead to the thrust enhancement observed in Fig. 5 (a), we examined the vortex structure in the wake and around the body of the fish, depicted in Fig. 6 (a and b). The wake generated from two undulating cycles, and vortices actively forming around the fish body in the third cycle are shown in Fig. 6 (a and b). A "double-row" [53] wake structure is observed in Fig. 6 (a), whereby vortex rings form at the tail and diverge laterally in the plane of undulation, typical of a carangiform swimmer at the current regime. Strong vortex cores form around the fish body. Leading edge vortices (LEVs) form on both the dorsal and ventral leading edges of the caudal fin, as shown in Fig. 6 (b). Anal fin vortex (AFV), formed due to the combining of the LEV and trailing-edge vortex (TEV) formed at the anal fin, is shed at the anal fin tip, advected downstream, and caught by the leading edge of the caudal fin to combine with its own LEV, as shown in Fig. 6 (b). At the trailing-edge of the caudal fin, TEVs are formed, and these connect with the LEVs to be shed together downstream. Typically, vortex rings or loops can form due to the linking of LEVs with each other and with TEVs and have been identified to be responsible for the propulsion of ray-fin fish swimming [31]. In Liu's study [6], vortex rings are clearly identified to contribute to creating thrust-producing backward-facing jets. In the current study, the trout's wide peduncle and a truncate caudal fin, contrasting crevalle jack's narrow peduncle and forked caudal fin, combined with differences in kinematics, may be responsible for the relatively laterally elongated vortex rings in the far wake shown in Fig. 6 (a). Such an elongated vortex ring has prominent counter-rotating vortex tubes (VTs) parallel to each other, formed due to LEV shedding from the CF leading edges. The paired VTs generate a strong backward-facing jet that is responsible for thrust production, as shown in Fig. 6 (c, d). The strength of the backward-facing jet production in M1, shown in Fig. 6 (c) is stronger than in M2, shown in Fig. 6 (d). The formation of VTs is identified to be crucial in thrust production, through which the underlying reason for the enhancement of C_T due to anal fin can be found.

In order to understand the capturing and interaction of different body parts and vortices that lead to the enhancement of thrust-producing VTs, the wake structures of M1 and M2 are depicted sequentially at various timesteps in Fig. 7 and Fig. 8, with the main vortices labeled. The red dashed lines trace the vortices with red arrows

indicating the direction of rotation of the vortices using a right-handed system. Text labels of abbreviations of vortex names are attached to the red dashed lines. Caudal fin leading-edge vortices are labeled with the abbreviation LEV, and leading-edge vortices formed on the anal fin are labeled with AF-LEV. Due to the complexity of vortex forming, shedding and interactions within an undulating cycle, subscripts "l" and "r" are used to differentiate between vortices that originate in the left-ward stroke and right-ward stroke, following the convention set by Liu et al, and Menzer et al. [6,49]. To visually aid this differentiation, text labels of vortices formed during the right-ward stroke are also colored blue. Superscripts "d" and "v" are used to differentiate the leading-edge vortices and vortex tubes formed on the dorsal and ventral sides of the fish.

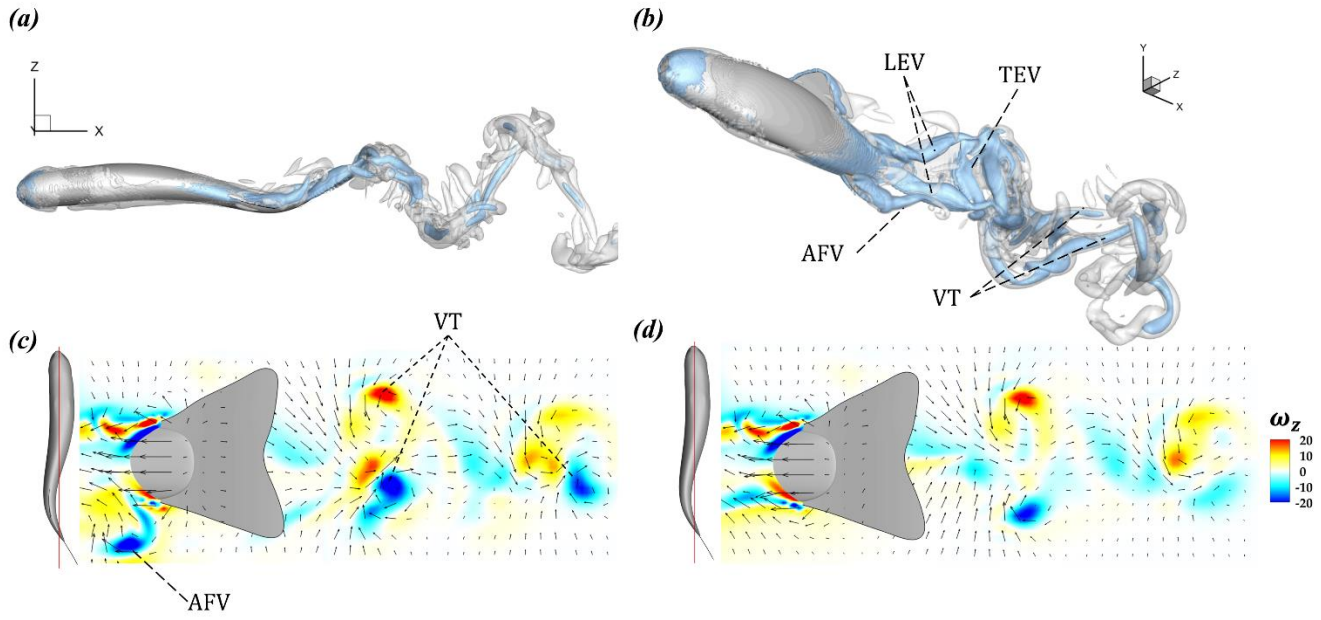

FIG. 6: Wake structure and vortex shedding with Q-criterion isosurfaces at $t/T = 0.18$ shown in (a) ventral view, and (b) perspective view, for $Q = 50$ (blue) and $Q = 5$ (white, transparent), and z-vorticity, ω_z, of (c) M1 and (d) M2 at the plane denoted by the red line.

The formation and shedding of $\mathrm{LEV^d}$, and the formation of $\mathrm{VT_r^d}$, on the dorsal side of the fish body is largely similar between M1 and M2. Major differences are observed on the ventral side. In M1, AF-LEVs and AFVs are formed periodically on the leading edge and tip of the anal fin. Due to a heaving-pitching phase lead exhibited by AF relative to CF, AF-LEV formation precedes caudal fin LEV formation. The timestep depicted in Fig. 7 (a1) is during the right-ward stroke, but the $\mathrm{AF\text{-}LEV_l}$ is fully formed during the preceding left-ward stroke. The formation and origin of $\mathrm{AF\text{-}LEV_l}$ can be seen in Fig. 8 (c1). Due to the proximity between AF and CF, an extension of AFV is absorbed by LEV before the AFV is completely shed (Fig. 7 (a1)). At the timestep depicted in Fig. 7 (b1, b2), relatively high C_T values are observed in Fig. 5 (a) for CFs of both M1 and M2. Correspondingly, the $\mathrm{LEV_r^v}$s for both M1 and M2 are strong and coherent. M2's LEV is aided by the connected peduncle vortices (PV) while M1's LEV is enhanced by a slightly weaker PV and the interaction with AFV. In Fig. 7 (b1, b2), the LEVs for both M1 and M2 start to separate, corresponding to the dip in $C_{T_{CF}}$ in Fig. 5 (a).

CF's interaction with the shed AFV is depicted in Fig. 7 (b1) and Fig. 8 (c1). In M2, instead of AFV, PV is formed from the body shear layer in the absence of an anal fin. PV then combines with the similarly oriented LEV at the root of the caudal fin, as shown in Fig. 7 (a2, b2, c2). The anal fin in M1 diverts the body shear layer away from the body, leading to the formation of AF-LEV (Fig. 7 (a1)). AFV is formed through the combination of AF-LEV and other AF-bound vortices and shear layers at the AF tip. The subsequently shed AFV then interacts with the caudal fin at near the mid-chord point (chord defined as the length of CF measured from the root at the peduncle to the trailing edge), instead of the root, as shown in Fig. 7 (b1). The similarly oriented AFV and LEV combine to become a larger and stronger VT to be shed at the tip of the ventral edge of the caudal fin (Fig. 7 (c1)).

The combining of LEV and AFV lead to a stronger VT than the combining of PV and LEV. At the same time, AF-LEV_r forms and leads to the shedding of AFV_l, to interact with LEV_l. The development of VT_r^v following similar formation process during the left-ward stroke can be observed in Fig. 8 for both M1 and M2. AFV_r in M1 helps support and elongate the similarly oriented VT_r^v, so that it stays coherent till the end of the cycle. The PV_r^v that continuously feed into LEV^v enhances the VT_r^v in M2 in a similar manner. However, the strength and speed of PV_r^v seems insufficient to support VT_r^v for long durations, as demonstrated by the comparatively shorter VT_r^v in Fig. 8 (b2) than in Fig. 8 (b1). In contrast, AFV stays at least partially connected with VT^v for the entirety of the left-ward half cycle.

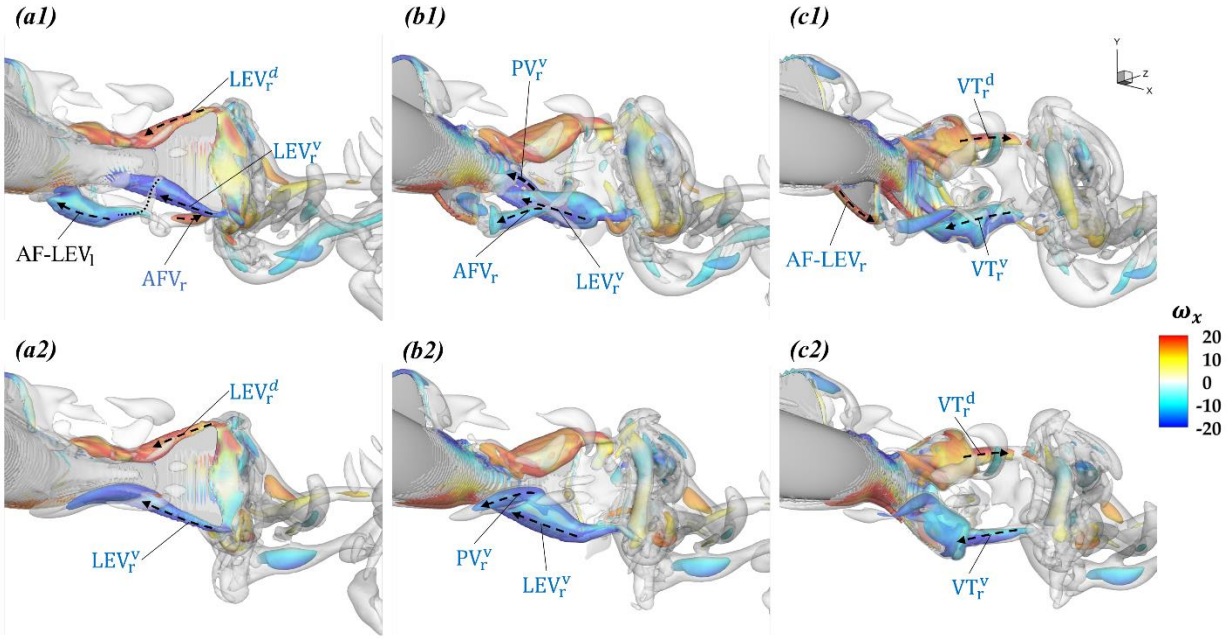

FIG. 7. Three-dimensional wake structures of M1 (a1, b1, c1) and M2 (a2, b2, c2) during caudal fin's left-right stroke, at timesteps (a) $t/T = 0.063$, (b) $t/T = 0.25$ and (c) $t/T = 0.44$. The wake structures are visualized by the isosurface Q-criterion, with Q = 50 (colored by streamwise vorticity contour) and Q = 5 (white).

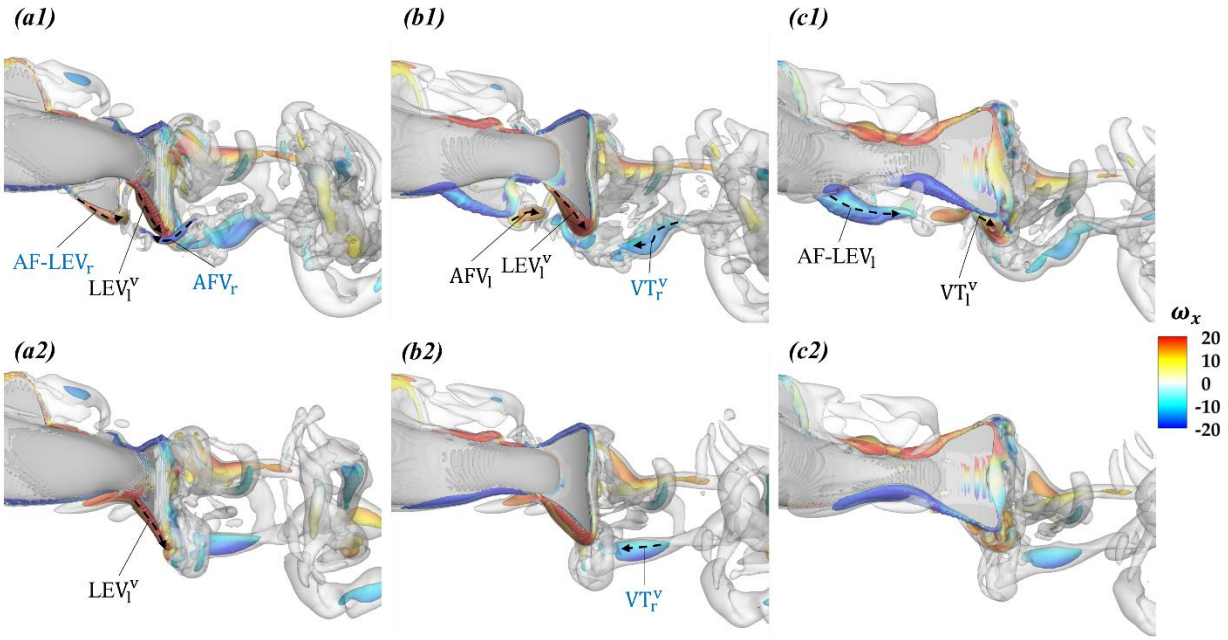

FIG. 8. Three-dimensional wake structures of M1 (a1, b1, c1) and M2 (a2, b2, c2) during caudal fin's right-left stroke, at timesteps (a) $t/T = 0.63$, (b) $t/T = 0.87$ and (c) $t/T = 1.00$. The wake structures are visualized by the isosurface Q-criterion, with Q = 50 (colored by streamwise vorticity contour) and Q = 5 (white).

Timesteps shown in Fig. 7 (c) and Fig. 8 (a) correspond to instances of large caudal fin C_T difference between M1 and M2. The vortices shed by the AF at these timesteps in M1, besides feeding into VT, also skirt along the ventral-side leading edge of the caudal fin. To further examine the mechanism through which the capturing of AFV enhances thrust produced by the CF, for timesteps of large $C_{T_{CF}}$ difference between M1 and M2, a slice cut is made to show the x-direction vortex strength in Fig. 9, near the location where CF intercepts AFVs. The time sequence selected here demonstrates that the dominant mechanism through which AFV enhances LEV_l^v is by helping its initiation. During this time, the caudal fin undergoes a reversal of flapping direction. The AFV produced during the rightward stroke rotates in the negative x direction, the same as the PV generated in M2. However, whereas the PV is located near the mid-span location of the CF, the AFV is underneath the leading edge of the caudal fin, an opportune placement because the shearing between the vortex and the CF leading edge causes a positive LEV_l^v to form more readily than M2. In Fig. 9 (a2), M2's LEV is absent due to the caudal fin being in a transitional stage and having a low angle of incidence in the flow, the LEV of M1 is already formed due to the shearing from AFV. In subsequent timesteps, LEV continues to grow in M1, and starts to form in M2, the result being consistently stronger LEV in the presence of AFV during the stroke-reversal stage, as seen in Fig. 9 (a1-c1) compared to (a2-c2).

A less measurable benefit of AFV, made apparent also by Fig. 9, is the avoidance of lateral jet formations due to channels existing between closely placed counter-rotating vortices, as denoted in Fig. 9 (a2). As mentioned before, the anal fin diverts the body shear layer away ventrally, as those vortices shed can more directly benefit the caudal

fin leading edge, whereas in its absence, vortices travel in towards mid-span region of the caudal fin. Dorsal PV and ventral PV congregate mid-span of the caudal fin to produce a channel between them, producing a laterally facing jet, labeled by a green arrow in Fig. 9 (a2). Though lateral jets are beneficial in maneuverability [29], when rectilinear propulsion is the goal, energy is wasted. The lateral jet in Fig. 9 (a2) can also resist the left-ward translation of the caudal fin, accounting for further energy expenditure. By diverting vortices to the outer edges of the caudal fin, this energy waste is avoided.

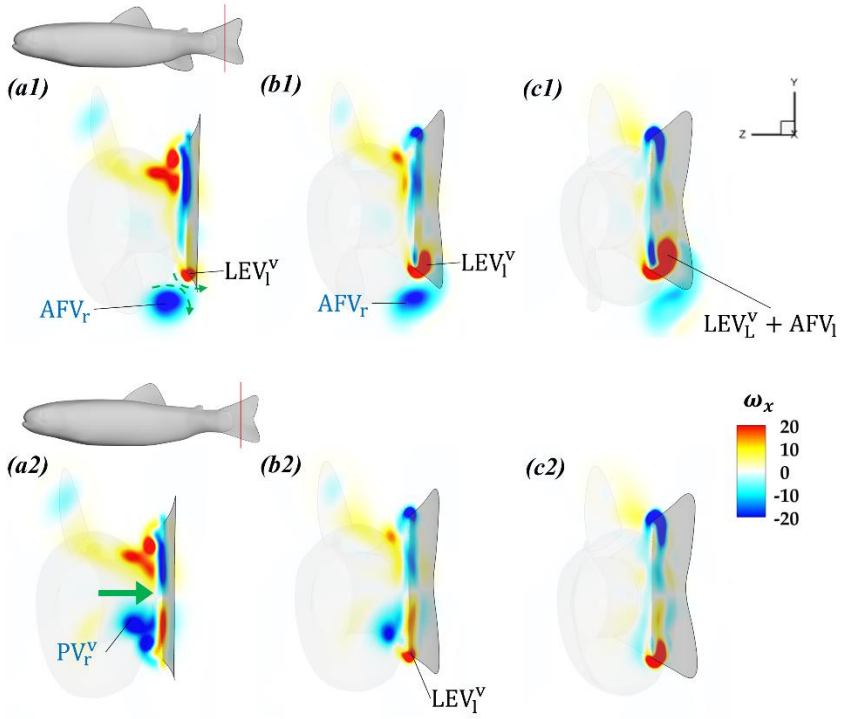

FIG. 9. Slice cut parallel to the yz-plane made at the location denoted by the red line in M1 and M2 shown in lateral view above (a1) and (a2), showing the x-vorticity, ω_x, for M1 (a1-c1) and M2 (a2-c2), at time steps (a1, a2) t/T = 0.44, (b1, b2) t/T = 0.50, and (c1, c2) t/T = 0.56. Green arrow indicating the direction of flow in a channel created by two closely set counter-rotating vortices.

To quantify the benefit of the AFV-LEV interaction described in Fig. 9, and ensure that it is not limited to the region near the slice-cut, a series of equally spaced slices are made along the entire CF leading edge at the time of stroke reversal and large CF thrust enhancement, to show the core of LEV_l^v, and the circulation strength of the core is calculated at the slice-cut locations. Figure 10 (a1-2) shows slices displaying ω_x contours with a cut-off value near the upper limit of the contour legend range shown in Fig. 9 to exclude auxiliary vortices and focus on only the core of the LEV_l^v. In Fig. 10 (b), the circulation strength ($|\Gamma|$) is non-dimensionalized by the product of free-stream velocity (U_∞) and (L_B). M1's LEV cores are larger than those of M2 along the whole CF leading edge. The circulation plot shown in Fig. 10 (b) confirms this visual observation, as the circulation strength at each station except the tip-bound one is higher in M1 than in M2. The difference is especially large near the middle of the space between the root and the tip. Whereas the LEV circulation plot for M2 exhibits a quadratic pattern, whereby it is

the strongest at the root and quickly drops off and levels out as we move further downstream, the LEV circulation plot for M1 exhibits a more linear pattern, the decreasing of the LEV circulation as the station is moved nearer the tip is less drastic. In this timestep, both LEV_l^v initiation due to AFV_r and absorption of AF-LEV_l extension by LEV_l^v are in effect at different locations, causing a uniform circulation enhancement along the entirety of CF leading edge.

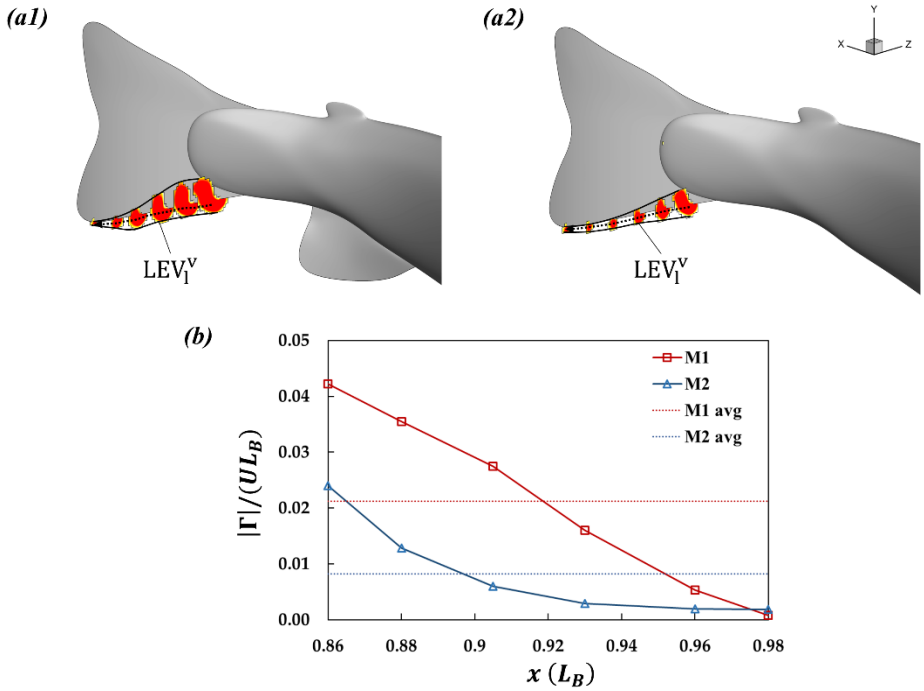

FIG. 10. At time step $t/T = 0.50$, 6 equally spaced x-slices made on the CF from near the root ($x = 0.86\ L_B$ from the trout's snout) to near the tip ($x = 0.98\ L_B$) showing dominant vortex formations on (a1) M1 and (a2) M2, with the cores traced by directional dotted lines indicated also the direction of rotation, the solid black lines denoting the boundaries of LEVs. The strengths of the LEVs on the slices are plotted in (b).

Next, to get from fluid physics back to forces on the body, pressure contours are depicted on a slice cut, the position of which is shown in Fig. 11 (a1, a2) top-left corner, intersecting part of the trunk, the anal fin, and quarter-span of the caudal fin. The time step shown in Fig. 11 (a-b), $t/T = 0.50$, corresponds to the instant where large thrust enhancement is observed in Fig. 5 (a). The pressure contour shown on the y-slice shows that the two opposite sides of the caudal fin are dominated by contrasting pressure-suction pressure fields, the region to the left of the caudal fin is predominantly positive (pressure), while the left side is predominantly negative (suction). Due to the orientation of the caudal fin, the pressure and suction sides lean downstream and upstream of the caudal fin, a configuration conducive to thrust production. Following the trajectories of the contour lines separating positive and negative pressure regions in Fig. 11 (a1, a2), one observes that more "leaching" of suction region occurs in M2, due to fluid's tendency to flow from high-pressure region to regions of negative pressure, reducing the overall pressure gradient. In contrast, the AF in M1 can preserve the pressure gradient better by preventing the crossflow of fluid from the positive-pressure to negative-pressure side of the body, leading to the stronger and more expansive suction

region in M1 compared to M2. The overall result is a larger lateral pressure gradient across M1's CF, leading to more forward thrust produced by the CF in M1 than in M2. Caudal fin surface pressure contours of M1 and M2, depicted in Fig. 11 (b1) and (b2), show that the comparative expansiveness of the region with high suction force in M1 is not limited to the leading edge of the caudal fin, but also extends to much of the ventral surface of the caudal fin. Due to the orientation of the caudal fin, the larger high-suction region on the CF surface in M1 compared to M2 also contributes to higher forward thrust force. The trajectory of contour lines separating negative and positive pressure regions in Fig. 11 (a1, a2) also suggests the other functions of AF, in reducing body drag and producing AF thrust, as the downstream side of AF and TK in M1 is consistently positive in pressure, whereas the negative pressure resides downstream of the TK in M2.

To further illustrate body-drag reduction and AF thrust production, pressure isosurface and full-body surface pressure contour for both M1 and M2 are shown in Fig. 11 (c-d) for the timestep $t/T = 0.88$, when a large difference in body drag and non-negative AF thrust is observed in Fig. 5 (a). The upstream surface of the peduncle region is predominantly negative pressure in both M1 and M2. But the AF in M1 can extend the negative-pressure region a bit further forward and enhance the bottom edge of that region, as seen by the more coherent negative-pressure isosurface in Fig. 11 (c1). The high suction force upstream of the trunk and the AF helps reduce drag on those body parts. In the body surface contour (Fig. 11 (d1, d2)), on the other side of the body, though the anterior portion looks similar, the pressure-side of the posterior region is stronger and more expansive in M1 than in M2. Whereas the high-pressure force is limited to near the middle of the fish's right-side surface in M2, with the suction force creeping over from the other side at the ventral edge, in M1, the high-pressure region extends from the dorsal to the ventral edge of the entirety of the posterior surface. This is also due to the lack of lateral crossflow due to the obstruction provided by the AF. The downstream side of the AF is also dominated by high-pressure, leading to thrust production by the anal fin.

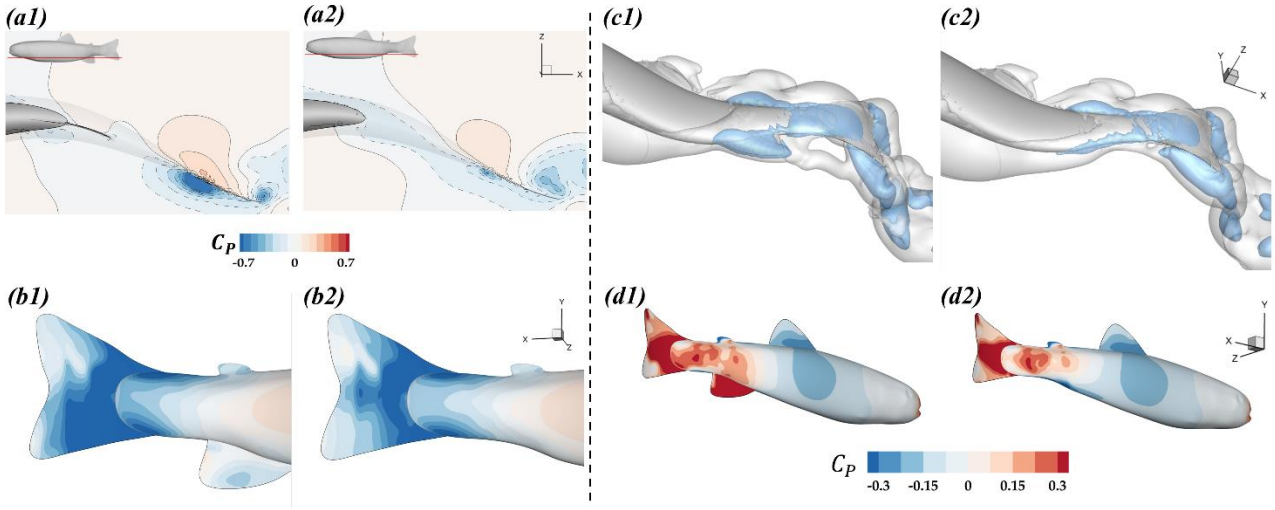

FIG. 11. Pressure plots at (a-b) $t/T = 0.50$ and (c-d) $t/T = 0.88$, with (a) a slice cut through the lower body, the precise position denoted in (a1), (a2) top-left corner with a red line, and dashed contour lines separating regions with negative pressure, (b) surface pressure on the suction side of the peduncle-CF section, (c) pressure isosurface with $C_P = -0.20$ (blue) and $C_P = -0.05$ (white), and (d) surface pressure contour of the whole right side of the fish body on (a1, b1, c1) M1, and (a2, b2, c2) M2.

B. Effect of AF-CF spacing

Different fish species and trout individuals may exhibit body shapes and morphologies differing from the ones of the individual used for analysis thus far. This section explores the dependence of vortex-fin interaction on the spacing between AF and CF. With the definition of d shown in Fig. 2 (b1) and d_0 denoting the AF-CF spacing in the baseline model, cases are run with d/d_0 varying from 0.75 to 1.50, and comparisons are made to the baseline case (M1) of $d/d_0 = 1$. The analysis in this section will focus on body parts most affected by AF, including AF itself, CF, and TK. The cycle-average thrust coefficient, $\bar{C}_T$, of different body parts in different cases is summarized in Table II. The trend of $\bar{C}_T$ as d/d_0 changes is shown in Fig. 12 (b). In Zhang et al. [25] the optimal range of spacing and relative heaving phase between tuna-inspired median and caudal fins that induced desirable vortex interaction was found to encompass the configuration of a real tuna. Similarly, the performance peak in the current study is found at $d/d_0 = 1$, indicating the original, anatomically realistic configuration on the biological fish as optimal for forward propulsion. The fish's AF position induces this optimum by striking a balance between thrust enhancement and drag reduction. The instantaneous C_T for TK, AF, and CF over a full cycle, shown in Fig. 12 (a), reveals that all three body parts are affected by the changing position of AF. As AF-CF spacing is decreased, with the AF moving more posterior, AF's thrust production is expected to increase due to the posterior body having a larger undulation amplitude, as determined by the fish's undulation envelope, leading to larger pitching-heaving amplitudes for AF. The simulation result shown in Fig. 12 (a), with the $C_{T_{AF}}$ line of $d/d_0 = 0.75$ being overall higher than that of $d/d_0 = 1.0$, agrees with expectation.

For trunk drag, significant variation from baseline is observed in the $d/d_0 = 1.50$ configuration, with the AF being more anterior. Although slightly less drag-inducing at the beginning of a stroke (half cycle), for most of a stroke, in $t/T = (0.15, 0.5)$ and $t/T = (0.65, 1.0)$, the trunk in the $d/d_0 = 1.50$ configuration produces more drag than in the baseline case. From the $\bar{C}_T$ summary shown in Table II, it can be calculated that the trunk drag is increased by 15.0% by changing d/d_0 from 1.0 to 1.50 and 0.85% by changing d/d_0 from 1.0 to 0.75. The original positioning of AF provides more significant trunk drag reduction than a more anteriorly positioned AF (larger d/d_0), and further decrease of AF-CF does not provide significant additional trunk drag reduction. For the caudal fin, the most drastic difference in instantaneous C_T between configurations with an anterior AF (large d/d_0) and a posterior AF (small d/d_0) occurs at the peaks of thrust production, when $t/T = 0.13$ during the rightward stroke, and $t/T = 0.63$ during the leftward stroke. A more anteriorly placed AF brings about higher peak CF C_T, with a clear separation among cases with d/d_0 values of 1.50, 1.0, and 0.75. A less significant difference is observed during stroke reversal, like the difference between the CF C_T curves of M1 and M2, most representatively at $t/T = 0.44$, with a trend that is the opposite of the thrust enhancement at CF C_T peaks. The largest improvement from baseline in CF $\bar{C}_T$ is achieved with $d/d_0 = 1.25$. The cycle averaged CF thrust coefficient, $\bar{C}_{T_{CF}}$ is 0.501 for $d/d_0 = 1.25$, and 0.482 for $d/d_0 = 1.00$, resulting in an overall improvement of 3.9% CF thrust, benefiting from thrust enhancements both in stroke reversal and at the peaks of thrust production. The difference occurring at the thrust reversal observed in Fig. 12 (a) is likely the result of the same vortex interaction causing the difference in CF thrust production between M1 and M2 observed in Fig. 5 (a), examined in section 3.1. Next, the flow physics causing significant variations in trunk drag reduction and CF thrust enhancement during a stroke are examined separately.

Table II. Summary of hydrodynamic performance: cycle-average coefficient of thrust.

$\boldsymbol{d/d_0}$	0.75	1.0	1.25	1.50
TK $\bar{C}_T$	-0.236	-0.234	-0.246	-0.269
AF $\bar{C}_T$	0.0475	0.0267	0.00955	-0.00150
CF $\bar{C}_T$	0.444	0.482	0.501	0.491

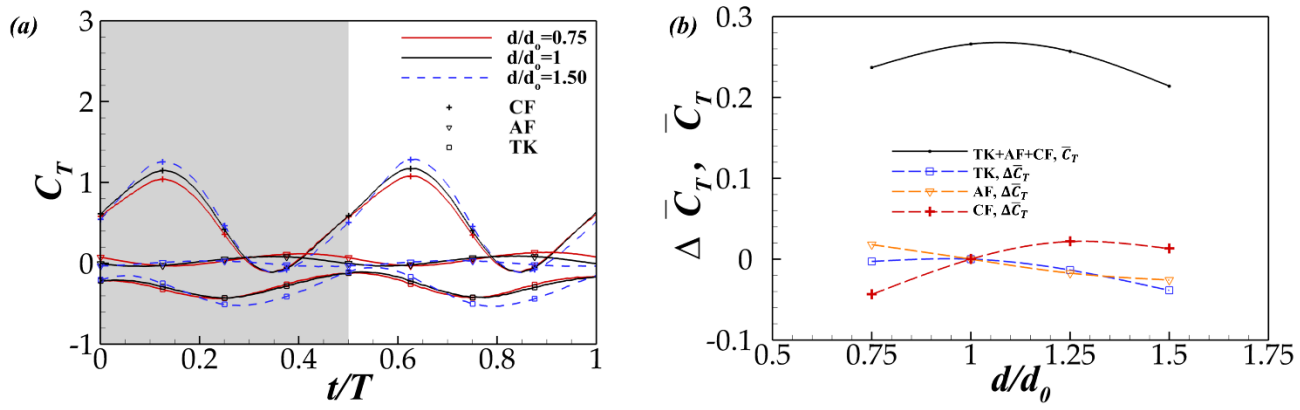

FIG. 12. (a) Time history of instantaneous C_T over a typical cycle for varying AF-CF spacing. (b) Performance trend in terms of cycle-averaged coefficient of thrust ($\bar{C}_T$) for the sum of body parts and deviation from baseline case ($\Delta\bar{C}_T = \bar{C}_T - \bar{C}_{T_{M1}}$) for individual body parts with respect to AF-CF spacing, d/d_0.

To explain the reduction of trunk drag due to moving AF more anterior from a fluid physics standpoint, pressure isosurfaces in flow around the fish and pressure contour on the surface of fish's body are plotted in Fig. 13 for cases with posterior-most ($d/d_0 = 0.75$) and anterior-most ($d/d_0 = 1.50$) AF. Extreme cases are chosen for comparison to highlight the flow phenomenon. The pressure on and around the dorsal fin and the anterior half of the fish trunk are unaffected by the varying position of AF. In the posterior region, near the peduncle, the anal fin helps maintain and expand the suction region on the upstream side. A comparison of pressure isosurfaces shown in Fig. 13 (a1) and (a2) elucidates the expansion and improved coherence of suction region in the fluid ahead of the peduncle. The surface pressure contour in this region on the pressure side also shows an expansion and more coherence of regions of desirable pressure force due to a more posterior AF. Whereas in the $d/d_0 = 1.50$ configuration, the bottom of the peduncle shows an extension of the negative pressure from the suction side, and a reduction of the desirable positive pressure region, the peduncle in the $d/d_0 = 0.75$ configuration has positive pressure residing across the entirety of the surface on the right side. Overall, the benefit of a more posterior AF in terms of trunk drag reduction is in preventing cross flow that can occur due to the narrowing of the trunk shape at the peduncle region, and thus maintaining the beneficial pressure gradient across the peduncle.

The added benefit of a more posterior AF, that of high thrust production by the AF itself, can also be explained here. The pressure isosurface on the AF shows a more coherent suction region on the leading edge of the further upstream side of the AF. This indicates not only a stronger forward-pointing suction force, but also a stronger AF-LEV, both leading to higher $C_{T_{AF}}$ observed in Fig. 12 (a) at the instant depicted in Fig. 13. The surface pressure contour on the downstream side of the AF in the more posterior case also shows an expansion and enhancement of positive pressure on AF.

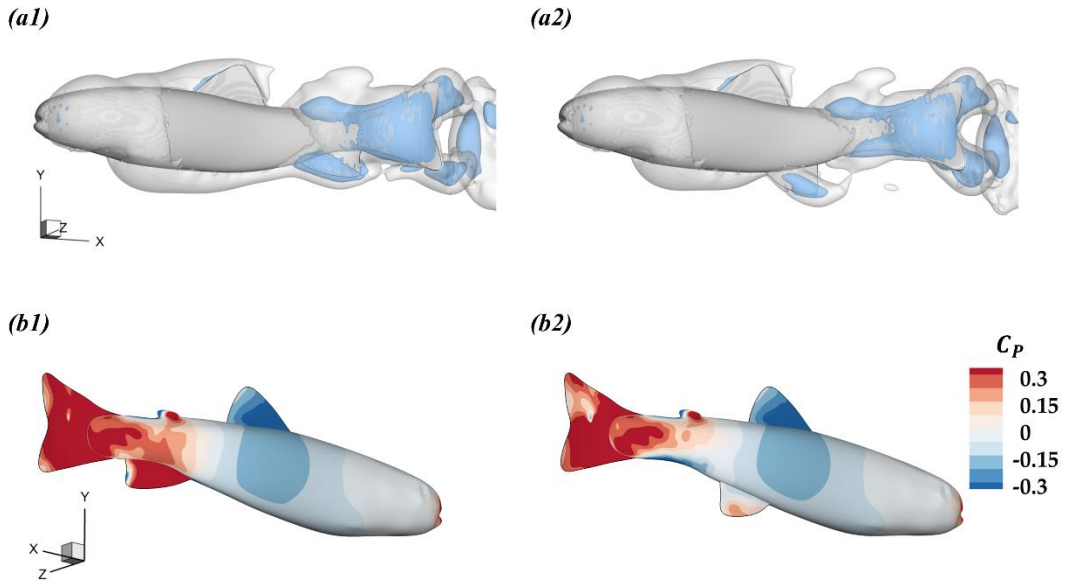

FIG. 13: (a) Pressure isosurface at t/T = 0.88, with $C_P = -0.05$ (white, transparent) and $C_P = -0.20$ (blue), (b) pressure contour on fish body at the same time step, for (a1, b1) $d/d_0 = 0.75$ and (a2, b2) $d/d_0 = 1.50$.

Next, we examine the effect of anal fin placement on the caudal fin's thrust production and explain variations in CF's C_T curve seen in Fig. 12 (a) from a flow physics standpoint. The interactions of AF-bound and CF-bound vortices, at a timestep of significant difference in instantaneous CF C_T are depicted in Fig. 14 for the extreme cases. Like M1 shown in Fig. 7 and Fig. 8, AFVs form around the anal fin and are shed periodically during flapping in all the AF locations tested. When the AF and CF are positioned close to each other, such as in the configuration shown in Fig. 14 (a), the flapping phases of AF and CF are also similar, so that the production of AF-LEV and LEV would be close to synchronous. In comparison, with a larger d/d_0, as shown in Fig. 14 (b), though the same coherent and attached LEV tubes can be seen on the leading edge of caudal fin, no AF-LEV can be clearly identified. Instead, a detached AFV has been shed from the anal fin and advected downstream. Ample spacing between the AF and the CF in the $d/d_0 = 1.50$ case allows for the full development of the PV, amplifying the LEV at the CF root through their connection. In contrast, in the $d/d_0 = 0.75$ case, the AF is placed in the narrowing peduncle interrupting the formation of PV. The shed AFV in the $d/d_0 = 0.75$ case runs parallel with the CF without interception and does not enhance the similarly rotating LEV.

The flow around the narrowing, streamlined peduncle causes the AFV to be advected up towards the caudal fin in the $d/d_0 = 1.50$ case. The subsequent constructive interaction between AFV and CF LEV is next examined. As shown in Fig. 14 (b) and Fig. 15 (a2), in the $d/d_0 = 1.50$ case, the LEV generated during the rightward stroke interacts with the AFV originating in the leftward stroke. As a result, the $\mathrm{AFV_l}$ rotates counter to $\mathrm{LEV_r}$, and stabilizes it at the peak of thrust production. At the same timestep, in the $d/d_0 = 0.75$ case, both $\mathrm{AFV_l}$ and $\mathrm{AFV_r}$ affect the formation of $\mathrm{LEV_r}$, as shown in Fig. 15 (a1). Consistent with the observation from Fig. 14 (a), the cores of $\mathrm{AFV_r}$

and LEV_r remain separate. The close proximity between the counter-rotating AFV_l and AFV_r cores facilitate a jet forming between them, pointing downwards, and destabilizing LEV_r by pulling it away from the CF. The strong and stable LEV_r in the $d/d_0 = 1.50$ case eventually forms a strong VT to have a lasting effect even as it is shed downstream. A narrowing of the space between the vortex tubes is observed in Fig. 14 (b), with VT_r^v moved up closer to the VT from the dorsal side, towards the left end of the tubes. The proximity of counter-rotating vortices can be more stable and generate a stronger and more concentrated jet between them. Figure 15 (b1) and (b2) confirm that the core of VT_r^v is indeed stronger for $d/d_0 = 1.50$ than for $d/d_0 = 0.75$, due to PV enhancement and AFV stabilization of LEV in the anterior-AF case. With little difference in the VT from the dorsal side, the combined effect of VT_r^v being stronger and closer to the body midline is a stronger jet, as indicated by the field of vectors with large amplitudes in the space between the two vortex tubes.

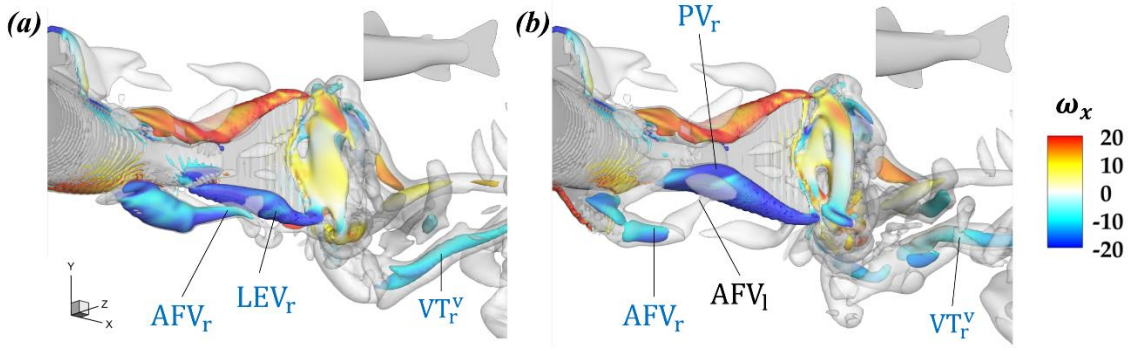

FIG. 14. 3-D wake structure visualized by the isosurface Q-criterion, with Q = 50, colored by streamwise vorticity (ω_x) contour, and Q = 5 (white) for (a) $d/d_o = 0.75$. (b) $d/d_o = 1.50$, at t/T = 0.13.

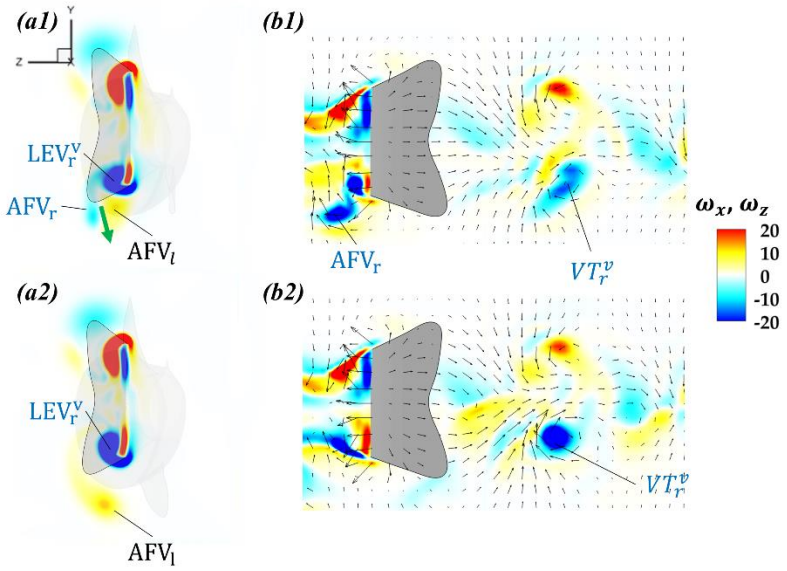

FIG. 15. (a), (b) ω_x and ω_z showing on the slicecut made at the same location as in Fig. 9 and Fig. 6 (c-d) at $t/T = 0.13$. (a1, b1) $d/d_o = 0.75$. (a2, b2) $d/d_o = 1.50$.

More desirable AF-CF interaction occurring when the distance between the two fins is increased is a surprising finding. However, a justification can be found by considering the phase difference between AF and CF. For this, we need to not only consider the flapping phase difference between the two fins, but also, the finite and varying distance between the fins determines that the vortex capturing is also phase shifted. In other words, the vortex shed from AF tip takes a finite time to reach the CF, and by then CF's flapping phase would have changed from the time when the AFV is shed. This phase shift due to the time it takes for AFV to travel from AF to CF needs to be considered. A glance at Fig. 16 (a) reveals that the flapping phase (in terms of lateral excursion of the fin tips) increases as the AF is moved further away from CF; the posterior AF has a curve closer in phase with CF tip, while the anterior-most AF has a curve more shifted in phase compared with the CF tip. Then we borrow the "global phase" (ϕ^*) definition developed by Kinsey and Dumas [18]. A variation of this phase definition has been used by Ribeiro et al. [15] to extract a coherent trend in the wake-foil interaction of tandem flapping foils. In this definition, the distance the vortex has to travel is defined by the x-distance between the AF tip and CF tip ($x_{CF_{tip}} - x_{AF_{tip}}$), and normalized by the convection speed of the vortex, approximated as the incoming flow speed, U_∞, and the flapping period T. Greek letter ψ is used to represent the flapping phase, the phase difference in lateral excursions of the CF and AF tips (Fig. 16 (a)) between AF and CF. Then the global phase, ϕ^*, is defined by equation (6).

$$\phi^* = 2\pi \frac{x_{CF_{tip}} - x_{AF_{tip}}}{U_\infty T} + \psi \tag{6}$$

The resulting global phases of the four AF-CF spacing varying cases are shown in Fig. 16 (b). This trend corresponds well with the general trend of increasing peak thrust coefficient, $C_{T_{\max}}$, as d/d_0 increases shown in Fig. 12 (a). The value of ϕ^* of the $d/d_0 = 1.25$ case being close to 2π ($0.997 \times 2\pi$) indicate a good synchronization in this case between the shedding of AFV and the capturing of it by CF, corresponding well with the observation that CF C_T reaches a peak when $d/d_0 = 1.25$ in Fig. 12 (b).

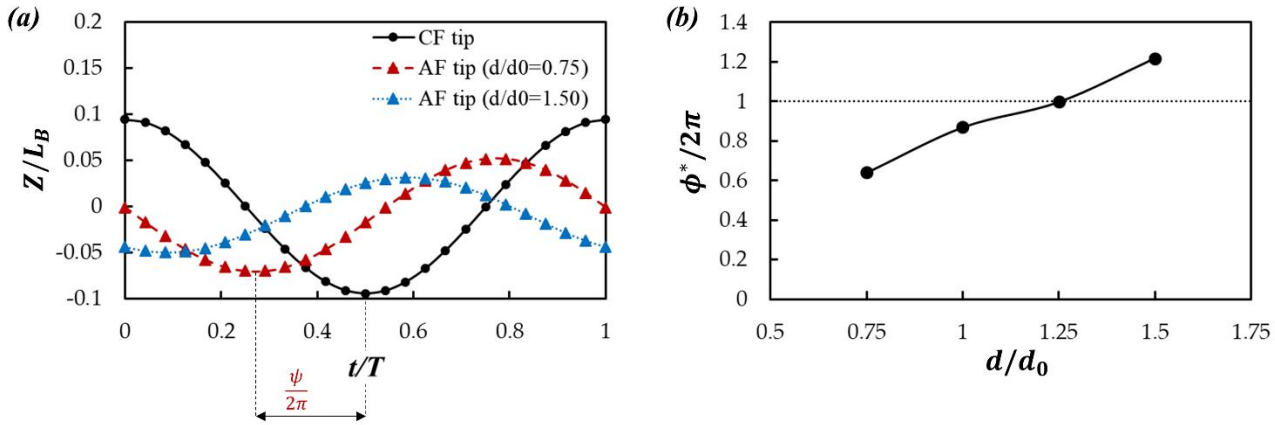

FIG. 16. Relative flapping motion of the AF and CF at different locations. (a) the lateral excursion of the CF tip and AF tip was tracked for an entire cycle, showing cases of the maximum and minimum AF-CF spacings for AF. (b) the global phase difference between AF and CF for different AF-CF spacing cases.

With anal fin's effects on trunk drag force reduction and caudal fin thrust force generation explored, and anal fin's own auxiliary thrust production considered, summing all these effects together, the original position of AF is found to be the most conducive to forward propulsion, as shown in Fig. 12(b).

C. Effect of varying AF height

By varying the height of the anal fin, while keeping the leading-edge arc length l_{AF} constant, the opening and closing of anal fin are mimicked. Knowledge from this section can provide a better understanding of the reason behind the fish's spontaneous opening and closing of its anal fin, and inform the design of a hydrodynamically optimal underwater vehicle. The extreme cases tested in this study have anal-fin heights, b_{AF}, of 0.75 b_{AF_0} and 1.25 b_{AF_0}, where b_{AF_0} is the height of the anal fin in the anatomically accurate model (M1). AFs with varying heights are shown in Fig. 2 (b3). As a result of varying fin height, the surface area of the fin is also varied, corresponding well with observation in real fish [29]. The surface area variation is approximately proportional to variations in b_{AF}, with the largest anal-fin surface area $S_{AF} = 1.13\ S_{AF_0}$ corresponding to $b_{AF} = 1.25\ b_{AF_0}$, and the smallest $S_{AF} = 0.75\ S_{AF_0}$ corresponding to $b_{AF} = 0.75\ b_{AF_0}$. The scaling proportionality between anal-fin height and surface area when reducing the anal fin size corresponds well with the observation that the leading-edge arc remains the same shape and overall angle relative to the ventral edge of the trunk in Fig. 2 (b3). The changing of leading-edge arc shape and overall angle when increasing the size of the anal fin while keeping the arc length constant leads to the loss of scaling proportionality between anal-fin height and surface area. The aspect ratios (AR) calculated using $AR = b_{AF}^2/S_{AF}$ for the cases of $b_{AF}/b_{AF_0} = 0.75$, 1.0 and 1.25 are 0.86, 0.62 and 0.45, respectively.

The performance of the trunk and fins affected by the varying AF size is summarized in Table III. Increasing AF size leads to increased $\bar{C}_T$ in both AF and CF. Recalling that coefficient of thrust is calculated uniformly for all body parts using the surface area of the caudal fin, an increase in AF $\bar{C}_T$ directly corresponds to increase in thrust

force. This is expected, and discussed by Standen and Lauder [29], due to an increase in surface area. The TK and CF also receive benefits from increased AF height, as seen by the increase of $\bar{C}_T$ on both TK and CF rows, as b_{AF}/b_{AF_0} increases. However, on TK, AF, and CF, the increase of $\bar{C}_T$ from $b_{AF}/b_{AF_0} = 0.75$ to $b_{AF}/b_{AF_0} = 1.00$ is more drastic than the increase of $\bar{C}_T$ from $b_{AF}/b_{AF_0} = 1.00$ to $b_{AF}/b_{AF_0} = 1.25$, indicating a plateau in hydrodynamic force trend; though significant benefit is gained by opening the AF from a relatively closed position ($b_{AF}/b_{AF_0} = 0.75$) to the position exhibited by the model fish ($b_{AF}/b_{AF_0} = 1.00$), further opening of the AF rays by the same proportion (to $b_{AF}/b_{AF_0} = 1.25$) does not yield significant gains.

Increased surface area can also lead to a higher power requirement, as confirmed by the comparison of $\bar{C}_{PW}$ in Table III for TK, AF and CF. The largest variation is observed on the AF. A 27.3% decrease and 26.6% increase in AF $\bar{C}_{PW}$ is observed when AF height is reduced and increased by 25%, respectively. Propulsive efficiency (η) is calculated as $\eta = \bar{C}_T/\bar{C}_{PW}$, and it is optimized in the original, anatomically accurate model, whose $b_{AF}/b_{AF_0} = 1.00$. For the CF, steady increases of η is observed as b_{AF} is increased, though the increases are slight (~1% variation) and a plateau seems to approach. Overall, summing the effect of both propulsors, a performance peak exists in $b_{AF} \in (0.75, 1.25)b_{AF_0}$, near the anatomically accurate configuration.

Table III. Performance summary of varying anal-fin height, showing the cycle-average values of coefficient of thrust, coefficient of power and, for the propulsors (anal fin and caudal fin), the propulsive efficiency, calculated as the ratio of $\bar{C}_T/\bar{C}_{PW}$.

	b_{AF}/b_{AF_0}	$\overline{C}_T$	$\overline{C}_{PW}$	η
TK	0.75	-0.240	0.921	
	1.00	-0.234	0.932	
	1.25	-0.232	0.939	
AF	0.75	0.0181	0.0660	27.4%
	1.00	0.0268	0.0908	29.5%
	1.25	0.0334	0.115	29.0%
CF	0.75	0.468	0.855	54.7%
	1.00	0.482	0.865	55.7%
	1.25	0.489	0.869	56.3%
Sum	0.75	0.246	1.842	
	1.00	0.275	1.888	
	1.25	0.290	1.923	

IV. CONCLUSIONS

In this study, we explored the interaction of the fish's anal fin with other body parts, focusing on the vortex-fin interaction between the anal fin and the caudal fin. It is found that the LEV formed on the caudal fin aids in thrust production by (1) creating a forward-pointing suction force, and (2) when shed, forming counter-rotating vortex tubes that enhance the backward facing jet in the channel between the tubes. The anal fin is found to produce coherent leading-edge vortices that are separate from body vortices, and the thrust-type vortices shed from the anal fin also enhance the thrust production of the caudal fin. AFV from the anal fin encounters the leading edge of the CF during stroke reversal to help initiate and stabilize the caudal fin's LEV through the shearing between AFV and the caudal fin surface. In the presence of the anal fin, the caudal fin can produce stronger and longer-lasting ventral vortex tubes that are closer to the dorsal vortex tubes of the same cycle, resulting in a stronger and more focused backward-facing jet. An 8.6% enhancement of the caudal fin thrust is achieved in the presence of the anal fin. Through parametric studies, it is also revealed that by adjusting for the wake-capture phase difference between the

anal fin and caudal fin, AFV can also stabilize CF LEV in the middle of a tail stroke, resulting in enhancement of lift-based thrust production at the peaks of caudal-fin thrust generation. Combining both mechanisms, the anal fin at the optimal position provides an additional enhancement of caudal fin thrust compared to the baseline case.

Additional functions of the anal fin are found to include a reduction of trunk drag, and a small amount of thrust production. In the baseline case, a 18.6% decrease in trunk drag is attributed to the anal fin's blocking lateral cross flow and the loss of pressure gradient. The anal fin is also found to produce 5.3% of the total propulsive force in its original size and position. By adjusting the position of the anal fin along the fish trunk, different amounts of reduction in trunk drag and production of the anal-fin thrust are found, with a more posterior anal fin producing more thrust while maintaining trunk drag reduction, and a more anterior anal fin producing less thrust and less effective in reducing trunk drag. This, combined with the diminishment of CF thrust enhancement by an anal fin extremely close to caudal fin, due to vortex capturing phase shifts, the optimal position of the anal fin is the original, anatomically accurate configuration, wherein the net forward force of the full fish body is the highest. Similarly, by varying the height and shape of the anal fin to mimic its opening and closing, it is also found that the original anatomically accurate configuration is optimal for propulsive efficiency, defined as the ratio of the cycle-average coefficient of thrust and cycle-average coefficient of power.

The biological height and surface area of the anal fin of the fish is found to be optimal for forward propulsive efficiency in steady rectilinear swimming compared to other anal-fin configurations, via mechanisms elucidated in this paper. However, the role of the anal fin in maintaining lateral-directional stability and the ability of trout to active control the anal fin in coordination with the dorsal fin, paired fins and trunk remain interesting areas for future studies.

ACKNOWLEDGMENTS

Thanks to members of the Lauder Lab for assistance with fish care and with the trout kinematic and hydrodynamic experiments, and especially to Dr. Robin Thandickal for his insights and assistance with calculating and interpreting pressure on fish and robot body surfaces. Additionally, thanks to the University of Virginia Research Computing Group for the availability of the Rivanna supercomputing cluster. This research was supported by grants from the Office of Naval Research (N00014-14-1-0533 and N00014-15-1-2234), NSF Grant (093088-17158) to GVL, and CNS-1931929 to HD.

REFERENCES

[1] J. M. Anderson, K. Streitlien, D. S. Barrett, and M. S. Triantafyllou, *Oscillating Foils of High Propulsive Efficiency*, J Fluid Mech **360**, 41 (1998).

[2] M. J. Lighthill, Aquatic Animal Propulsion of High Hydromechanical Efficiency, 1970.

[3] M. S. Triantafyllou, G. S. Triantafyllou, and D. K. P. Yue, *Hydrodynamics of Fishlike Swimming*, Annu. Rev. Fluid Mech. 33 (2000).

[4] J. D. Eldredge and A. R. Jones, *Leading-Edge Vortices: Mechanics and Modeling*, Annu. Rev. Fluid Mech **51**, 75 (2019).

[5] G. Liu, H. Dong, and C. Li, *Vortex Dynamics and New Lift Enhancement Mechanism of Wing-Body Interaction in Insect Forward Flight*, J Fluid Mech **795**, 634 (2016).

[6] G. Liu, Y. Ren, H. Dong, O. Akanyeti, J. C. Liao, and G. V. Lauder, *Computational Analysis of Vortex Dynamics and Performance Enhancement Due to Body-Fin and Fin-Fin Interactions in Fish-like Locomotion*, J Fluid Mech **829**, 65 (2017).

[7] I. Borazjani and M. Daghooghi, *The Fish Tail Motion Forms an Attached Leading Edge Vortex*, Proceedings of the Royal Society B: Biological Sciences **280**, (2013).

[8] T. Y. Wu, *Fish Swimming and Bird/Insect Flight*, Annu Rev Fluid Mech **43**, 25 (2011).

[9] R. R. Harbig, J. Sheridan, and M. C. Thompson, *The Role of Advance Ratio and Aspect Ratio in Determining Leading-Edge Vortex Stability for Flapping Flight*, J Fluid Mech **751**, 71 (2014).

[10] C. Li, H. Dong, and K. Zhao, *A Balance between Aerodynamic and Olfactory Performance during Flight in Drosophila*, Nat Commun **9**, 3215 (2018).

[11] H. Dong and Z. Liang, *Effects of Ipsilateral Wing-Wing Interactions on Aerodynamic Performance of Flapping Wings*, in *48th AIAA Aerospace Sciences Meeting Including the New Horizons Forum and Aerospace Exposition* (American Institute of Aeronautics and Astronautics, Reston, Virigina, 2010).

[12] J. C. Liao, D. N. Beal, G. V. Lauder, and M. S. Triantafyllou, *Fish Exploiting Vortices Decrease Muscle Activity*, Science (1979) **302**, 1566 (2003).

[13] J. C. Liao, D. N. Beal, G. V. Lauder, and M. S. Triantafyllou, *The Kármán Gait: Novel Body Kinematics of Rainbow Trout Swimming in a Vortex Street*, Journal of Experimental Biology **206**, 1059 (2003).

[14] L. Kang, W. Cui, X.-Y. Lu, and H. Huang, *Hydrodynamic Force Induced by Vortex–Body Interactions in Orderly Formations of Flapping Tandem Flexible Plates*, Physics of Fluids **34**, 021901 (2022).

[15] B. L. R. Ribeiro, Y. Su, Q. Guillaumin, K. S. Breuer, and J. A. Franck, *Wake-Foil Interactions and Energy Harvesting Efficiency in Tandem Oscillating Foils*, Phys Rev Fluids **6**, 074703 (2021).

[16] I. Akhtar, R. Mittal, G. V. Lauder, and E. G. Drucker, *Hydrodynamics of a Biologically Inspired Tandem Flapping Foil Configuration*, Theor Comput Fluid Dyn **21**, 155 (2007).

[17] X. Shao, D. Pan, J. Deng, and Z. Yu, *Hydrodynamic Performance of a Fishlike Undulating Foil in the Wake of a Cylinder*, Physics of Fluids **22**, 111903 (2010).

[18] T. Kinsey and G. Dumas, *Optimal Tandem Configuration for Oscillating-Foils Hydrokinetic Turbine*, Journal of Fluids Engineering, Transactions of the ASME **134**, (2012).

[19] P. Han, Y. Pan, G. Liu, and H. Dong, *Propulsive Performance and Vortex Wakes of Multiple Tandem Foils Pitching In-Line*, J Fluids Struct **108**, (2022).

[20] A. S. Hegde, P. S. Gurugubelli, and V. Joshi, *Effect of Combined Heaving and Pitching on Propulsion of Single and Tandem Flapping Foils*, (2022).

[21] D. Rival, G. Hass, and C. Tropea, *Recovery of Energy from Leading- and Trailing-Edge Vortices in Tandem-Airfoil Configurations*, J Aircr **48**, 203 (2011).

[22] M. S. Triantafyllou, A. H. Techet, and F. S. Hover, *Review of Experimental Work in Biomimetic Foils*, IEEE Journal of Oceanic Engineering **29**, 585 (2004).

[23] M. Narasimhan, H. Dong, R. Mittal, and S. N. Singh, *Optimal Yaw Regulation and Trajectory Control of Biorobotic AUV Using Mechanical Fins Based on CFD Parametrization*, J Fluids Eng **128**, 687 (2006).

[24] J. W. Newbolt, J. Zhang, and L. Ristroph, *Flow Interactions between Uncoordinated Flapping Swimmers Give Rise to Group Cohesion*, Proc Natl Acad Sci U S A **116**, 2419 (2019).

[25] J. D. Zhang, H. J. Sung, and W. X. Huang, *Hydrodynamic Interaction of Dorsal Fin and Caudal Fin in Swimming Tuna*, Bioinspir Biomim **17**, (2022).

[26] J. D. Zhang and W. X. Huang, *Numerical Model and Hydrodynamic Performance of Tuna Finlets*, Theoretical and Applied Mechanics Letters **12**, (2022).

[27] J. Wang, D. K. Wainwright, R. E. Lindengren, G. V. Lauder, and H. Dong, *Tuna Locomotion: A Computational Hydrodynamic Analysis of Finlet Function*, J R Soc Interface **17**, (2020).

[28] C. D. Wilga and G. V. Lauder, *Locomotion in Sturgeon: Function of the Pectoral Fins*, Journal of Experimental Biology **202**, 2413 (1999).

[29] E. M. Standen and G. V. Lauder, *Hydrodynamic Function of Dorsal and Anal Fins in Brook Trout (Salvelinus Fontinalis)*, Journal of Experimental Biology **210**, 325 (2007).

[30] E. G. Drucker and G. V. Lauder, *Locomotor Function of the Dorsal Fin in Rainbow Trout: Kinematic Patterns and Hydrodynamic Forces*, Journal of Experimental Biology **208**, 4479 (2005).

[31] G. V. Lauder and P. G. A. Madden, Learning from Fish: Kinematics and Experimental Hydrodynamics for Roboticists, 2006.

[32] D. G. Matthews and G. V. Lauder, *Fin-Fin Interactions during Locomotion in a Simplified Biomimetic Fish Model*, Bioinspir Biomim **16**, (2021).

[33] P. Han, G. V. Lauder, and H. Dong, *Hydrodynamics of Median-Fin Interactions in Fish-like Locomotion: Effects of Fin Shape and Movement*, Physics of Fluids **32**, (2020).

[34] J. Zhu, C. White, D. K. Wainwright, V. Di Santo, G. V. Lauder, and H. Bart-Smith, Tuna Robotics: A High-Frequency Experimental Platform Exploring the Performance Space of Swimming Fishes, 2019.

[35] G. V. Lauder, P. Madden, I. Hunter, J. Tangorra, N. Davidson, L. Proctor, R. Mittal, H. Dong, and M. Bozkurttas, *Design and Performance of a Fish Fin-like Propulsor for AUVs*, in *Proceedings of 14th International Symposium on Unmanned Untethered Submersible Technology* (Lee, New Hampshire, USA, 2005).

[36] V. Di Santo, E. Goerig, D. K. Wainwright, O. Akanyeti, J. C. Liao, T. Castro-Santos, and G. V. Lauder, *Convergence of Undulatory Swimming Kinematics across a Diversity of Fishes*, Proceedings of the National Academy of Sciences **118**, (2021).

[37] G. V. Lauder, *Function of the Caudal Fin During Locomotion in Fishes: Kinematics, Flow Visualization, and Evolutionary Patterns*, Am Zool **40**, 101 (2000).

[38] L. Ferry and G. V. Lauder, *Heterocercal Tail Function in Leopard Sharks: A Three-Dimensional Kinematic Analysis of Two Models*, Journal of Experimental Biology **199**, 2253 (1996).

[39] R. Thandiackal and G. V. Lauder, *How Zebrafish Turn: Analysis of Pressure Force Dynamics and Mechanical Work*, Journal of Experimental Biology (2020).

[40] R. Thandiackal, C. H. White, H. Bart-Smith, and G. V. Lauder, *Tuna Robotics: Hydrodynamics of Rapid Linear Accelerations*, Proceedings of the Royal Society B: Biological Sciences **288**, 20202726 (2021).

[41] K. N. Lucas, G. V. Lauder, and E. D. Tytell, *Airfoil-like Mechanics Generate Thrust on the Anterior Body of Swimming Fishes*, Proceedings of the National Academy of Sciences **117**, 10585 (2020).

[42] R. Mittal, H. Dong, M. Bozkurttas, F. M. Najjar, A. Vargas, and A. von Loebbecke, *A Versatile Sharp Interface Immersed Boundary Method for Incompressible Flows with Complex Boundaries*, J Comput Phys **227**, 4825 (2008).

[43] A. Menzer, Y. Ren, J. Guo, B. W. Tobalske, and H. Dong, *Wing Kinematics and Unsteady Aerodynamics of a Hummingbird Pure Yawing Maneuver*, Biomimetics **7**, 115 (2022).

[44] C. Koehler, Z. Liang, Z. Gaston, H. Wan, and H. Dong, *3D Reconstruction and Analysis of Wing Deformation in Free-Flying Dragonflies*, Journal of Experimental Biology (2012).

[45] C. C. Lindsey, *Form, Function, and Locomotory Habits in Fish*, in (1978), pp. 1–100.

[46] M. S. U. Khalid, J. Wang, I. Akhtar, H. Dong, M. Liu, and A. Hemmati, *Larger Wavelengths Suit Hydrodynamics of Carangiform Swimmers*, Phys Rev Fluids **6**, 073101 (2021).

[47] M. S. U. Khalid, J. Wang, H. Dong, and M. Liu, *Flow Transitions and Mapping for Undulating Swimmers*, Phys Rev Fluids **5**, 063104 (2020).

[48] J. Wang, Y. Ren, C. Li, and H. Dong, *Computational Investigation of Wing-Body Interaction and Its Lift Enhancement Effect in Hummingbird Forward Flight*, Bioinspir Biomim **14**, 046010 (2019).

[49] A. Menzer, Y. Gong, F. E. Fish, and H. Dong, *Bio-Inspired Propulsion: Towards Understanding the Role of Pectoral Fin Kinematics in Manta-like Swimming*, Biomimetics **7**, 45 (2022).

[50] Q. Zhong, H. Dong, and D. B. Quinn, *How Dorsal Fin Sharpness Affects Swimming Speed and Economy*, J Fluid Mech **878**, 370 (2019).

[51] J. O. Dabiri, S. Bose, B. J. Gemmell, S. P. Colin, and J. H. Costello, *An Algorithm to Estimate Unsteady and Quasi-Steady Pressure Fields from Velocity Field Measurements*, Journal of Experimental Biology (2013).

[52] K. N. Lucas, J. O. Dabiri, and G. V. Lauder, *A Pressure-Based Force and Torque Prediction Technique for the Study of Fish-like Swimming*, PLoS One **12**, e0189225 (2017).

[53] I. Borazjani and F. Sotiropoulos, *Numerical Investigation of the Hydrodynamics of Carangiform Swimming in the Transitional and Inertial Flow Regimes*, Journal of Experimental Biology **211**, 1541 (2008).